Diagnostics and Therapy Assessment Using Label-Free Raman Imaging

Samir F. El-Mashtoly* and Klaus Gerwert

Cite This: https://doi.org/10.1021/acs.analchem.1c04483

Read Online

ACCESS | Metrics & More | Article Recommendations

CONTENTS

Raman microspectroscopy is an emerging analytical tool that can monitor the biochemical composition of biological or biomedical specimens, including proteins, cells, and tissues, as well as biofluids. All constituents of a biomedical specimen contribute to the Raman bands producing a complex Raman spectrum, which is a spectral readout of the integral biochemical status of the sample and represents a "molecular fingerprint". The Raman spectral image provides not only qualitative and quantitative biochemical information but also morphological information. Disease progression or infectious diseases can induce changes in the Raman spectra, produced as a result of alteration in the biochemical composition of the specimen. Thus, Raman microspectroscopy can detect differ-

ences or changes between cells or tissues collected from healthy donors and diseased patients. Such biochemical changes may serve as "spectral biomarkers", which can be monitored throughout disease progression.

Raman spectroscopy has several advantages over other methods used for diagnostics and drug discovery. In addition to its specificity, it is a label-free and noninvasive tool that can be applied *in vivo* due to advances in instrumental platforms over the past decade. Raman microspectroscopy can deliver nearly real-time molecular information, enabling clinical implementation and pharmaceutical applications. It is inexpensively opposed to other medical imaging methods, including magnetic resonance imaging (MRI), positron emission tomography (PET), and ultrasound, and is an objective and more desirable tool than diagnostic methods that suffer from inter/intra-observer dilemmas, such as histopathology. Raman microspectroscopy also provides higher spatial resolution than PET and MRI. It also requires easy sample preparation and is suitable for live-cell imaging in contrast to, for example, mass spectrometry imaging, which needs extensive sample preparation, restricting its utilization in live imaging.

The acquired weak Raman intensity is one of the main shortcomings of spontaneous Raman spectroscopy in comparison with the absorption of infrared light or fluorescence emission. This leads to a longer accumulation time, which improves the Raman signal-to-noise ratio. To significantly enhance the Raman intensity, other variants of Raman techniques were developed, including surface-enhanced Raman spectroscopy (SERS) and coherent Raman spectroscopy, such as coherent anti-Stokes Raman scattering (CARS) and stimulated Raman scattering (SRS). Such developments have enabled not only nearly real-time Raman imaging but may get a better detection limit of the biomolecule, improving diagnostic accuracy and evaluate new drug candidates.

Raman spectroscopy has been employed in various applications, such as resolving subcellular components, diagnostics, and drug pharmacokinetics studies. Chemometrics

or machine learning is the predominant approach for analyzing Raman spectral data in these applications. Numerous chemometric approaches have been applied, including unsupervised models, such as principal component analysis (PCA) and clustering techniques, while others have utilized supervised learning approaches, such as partial least-squares (PLS), linear discriminant analysis (LDA), support vector machine (SVM), and deep learning approaches. The advantages and disadvantages of various chemometric methods and the differences between them are not included in the scope of the current review, and comprehensive reviews on the details of chemometric methods can be found elsewhere.[1−4] The combination of Raman spectroscopic methods and chemometric models has been utilized for many research topics, especially in diagnostics. Reviews have also been published that address the applications of Raman spectroscopy for medical diagnostics and drug pharmacokinetics.[5−9] However, it is necessary to present an updated review.

This review aims to present the recent applications of Raman technologies in the areas of diagnostics and assessment of drug candidates for therapy. It provides a comprehensive review of manuscripts published since 2019. We briefly describe the main Raman spectroscopic techniques, including spontaneous Raman spectroscopy, resonance Raman (RR) spectroscopy, SERS, CARS, and SRS, and review biomedical diagnostics applications using different specimens, such as biofluids, including blood, saliva, urine, and tear samples, as well as tissue biopsies. Next, we discuss drug pharmacokinetics in single cells and skin, activities of drug nanocarriers, and cells for therapy. Finally, we conclude with a discussion of the prospective of Raman-based methods for diagnostics and drug discovery.

RAMAN SPECTROSCOPIC TECHNIQUES

Spontaneous Raman Microscopy. In 1928, C.V. Raman reported for the first time Raman spectroscopy, and for this discovery, he was awarded the Nobel Prize in 1930.[10] Raman spectroscopy is a laser-based spectroscopic tool for the characterization of molecular vibrations. The interaction of the laser light with a molecule leads to changes in the frequency of the incident photons of light so that the molecule is excited to a virtual state and then returns to its ground energy state by scattering radiation. Most of the scattered photons from a molecule are elastically scattered (Rayleigh scattering); in this case, the scattered photons have the same energy as the incident photons. Conversely, a small fraction of the photons ($\sim$1 in 10^8) is inelastically scattered, where the energy of the scattered photons differs from that of the incident photons.[11] This phenomenon is called Raman scattering or the Raman effect. If the frequency of the scattered photons is less than that of the incident photons, it is named Stokes−Raman-scattering, whereas anti-Stokes Raman scattering is entitled when the frequency of the emitted photons is higher than that of the incident.

Raman effect probes changes in the polarizability of a vibrating molecule under investigation. Raman peaks are produced when there is associated change in the polarizability of the chemical bond. Plotting the intensity of the detected Raman scattered light versus these frequencies produces a spectrum of the molecule. Thus, every molecule has distinctive Raman signatures that can be used as a molecular fingerprint. In the case of cells or tissues, the Raman spectrum contains Raman signals of cellular constituents, including proteins,

lipids, phospholipids, nucleic acids, and carbohydrates, providing an integral molecular vibrational profile. An excitation laser with a relatively low energy is applied to acquire the Raman spectrum and produces inelastic scattering of the vibrational modes of the molecule. Raman spectroscopy is a nondestructive and label-free technique that requires easy sample preparation. Further, when the measurements are performed in buffer or media, water causes minimum interference compared to infrared absorption, enabling biomedical and biological applications, such as cell and biofluid measurements. When Raman spectroscopy is combined with optical microscopy, an imaging tool with a high spatial resolution is obtained, allowing the visualization of subcellular organelles. Thus, Raman microspectroscopy is an appropriate tool for *in vitro* and *in vivo* biological research studies, ranging from cells to tissues and biofluids.

The pharmaceutical activity of drug candidates is considerably monitored utilizing fluorescently labeled drug molecules. One of the main advantages of fluorescence microscopy is the molecular specificity provided by fluorescence molecules. However, they are usually much larger than the drug molecules of interest and can considerably vary the drug's pharmaceutical activity. Raman spectroscopy has been used to visualize the cellular uptake and distribution of small-molecule drug candidates in cells. However, most of these studies were performed using high concentrations of small molecules to allow their detection. The major challenge here is to detect drug candidates in cells at physiological concentrations utilizing Raman microspectroscopy. The acquisition speed of the Raman images of cells is limited because Raman scattering is weak in nature. Therefore, other Raman-based methods were developed to overcome the limitations of acquisition speed and detection limit in spontaneous Raman spectroscopy.

Resonance Raman (RR) Spectroscopy. Raman signals can be enhanced once the laser excitation wavelength coincides or is close to that of the electronic transition of the molecule being investigated. This results in the enhancement of Raman signals by a factor of 10^3 to 10^4 compared to spontaneous Raman signals, which is called the resonance Raman (RR) effect.[12,13] This effect can improve both the sensitivity and selectivity of the selected chromophore. RR spectroscopy is extensively applied to study proteins and their conformations by monitoring chromophores, such as heme, in the visible region and aromatic amino acids in the UV region. It has also been applied for live-cell imaging to detect cytochrome c dynamics during apoptosis.[14] However, a high fluorescence background is a disadvantage of RR spectroscopy because it is accompanied by radiative decay from the electronically excited state. To overcome the fluorescence, a preresonance condition is applied, in which the laser excitation is chosen on the red side of the absorption spectrum. In addition, time-gated approaches, rejection of fluorescence via a temporal resolution of the Raman spectra, can also be applied. This is because fluorescence emission is orders of magnitude slower than Raman scattering.[15]

Surface-Enhanced Raman Spectroscopy (SERS). Raman signals are significantly enhanced, up to $\geq 10^6$ orders of magnitude, once the molecule is adsorbed or located near rough metal or metal nanostructures of silver, gold, or copper.[16,17] This phenomenon is known as SERS, and it was discovered more than 4 decades ago.[18] SERS enhancement allows for the detection of very low concentrations of molecules of interest, enabling even single-molecule detection,

which is a clear advantage for diagnostic and therapeutic applications. Electromagnetic enhancement is the major contributor to the SERS enhancement, while chemical enhancement has some contribution, up to 10−100 times.[19] On the one hand, electromagnetic enhancement is due to an enhancement in the electric field that is provided by the interaction of incident electromagnetic radiation with the surface plasmons excited at the surface of the structure. On the other hand, chemical enhancement is attributed to charge transfer between the adsorbed molecule and the metal. Ag and Au are usually employed for SERS experiments because their surface plasmon resonance wavelengths are located within the visible and near-IR regions. Thus, they are suitable for SERS enhancement.[16,17]

Coherent Raman spectroscopy. Coherent Raman spectroscopy (CRS) is based on nonlinear effects. Thus, the speed and spatial resolution of CRS methods are above that of spontaneous Raman spectroscopy. Coherent Raman microscopic methods, such as CARS and SRS, use two short-pulse laser beams, pump (ω_p) and Stokes (ω_s) lasers, focused onto a sample. When the frequency difference between the pump and Stokes lasers ($\Delta\omega = \omega_p - \omega_s$) is in resonance with a specific molecular vibrational mode at a frequency (ω_{vib}), the Raman signal can be significantly enhanced in the CARS and SRS processes.[20,21] CARS is a four-wave mixing process, in which the molecule absorbs another pump photon and relaxes by emitting a strong blue-shifted anti-Stokes signal at frequency $\omega_{AS} = 2\omega_p - \omega_s$. One shortcoming of CARS is that it also takes place in nonresonant conditions, producing a high background, causing spectral distortion and artifacts.[22]

Regarding SRS, the Stokes and pump beams suffer stimulated Raman gain (SRG) and stimulated Raman loss (SRL), respectively. By modulating either Stokes or pump beams utilizing, for example, an electro-optic modulator, the gain or loss of photons is detected by a lock-in amplifier providing contrast to produce images at specific vibrational frequencies. When the frequency difference, $\Delta\omega$, does not resemble a molecular vibrational mode, SRG and SRL do not happen, resulting in SRS being completely nonresonant-background free, in contrast to CARS. In addition, SRS only replicates the spontaneous Raman spectrum, allowing quantitative analysis.[6,23]

Hyperspectral CRS microscopy has been established by tuning the pump laser in most cases over a range of the wavelength of interest; however, it often takes several minutes.[24,25] To overcome this problem, faster methods, such as multiplex/broadband CRS microscopy, have been developed using femtosecond lasers, where the coherent Raman spectrum is immediately acquired at each pixel within microseconds.[26,27] Such developments indicate that fast spectral images can be acquired for cells and tissues, which are suitable for clinical and pharmaceutical applications.

■ RAMAN SPECTROSCOPY FOR DIAGNOSTICS

Raman Spectroscopy of Biofluids. Body fluids allow minimally invasive diagnostics for several diseases. These samples are easy to collect from patients, permit collection several times, and are rich in biochemical information. In addition, body fluids, such as blood, urine, sputum, cerebrospinal fluid (CSF), saliva, and tears, may provide a rapid diagnostic and cost-effective approach.[28] Therefore, diagnosis based on body fluids has the potential to be employed in the healthcare system. Several studies have employed Raman spectroscopic methods using body fluids to diagnose various diseases, such as cancers, neurodegenerative diseases, and infectious diseases. These studies, published during and after 2019, are reviewed here.

Cancer Diagnostics. Noninvasive cancer diagnosis includes the identification of cancer biomarkers or circulating tumor cells in biofluids. Several reports have been dedicated to the detection of different cancer types using biofluids.

Gastric Cancer. Aslam et al. investigated the application of SERS in saliva samples collected from patients with gastric cancer ($n = 104$) and healthy controls ($n = 116$).[29] An artificial neural network (ANN) of the SERS spectra showed that changes in 10 amino acid biomarkers enabled identification of cancer patients with an accuracy of 92.27%, a sensitivity of 94.8%, and a specificity of 90.2%.[29] Furthermore, Bahreini et al. employed spontaneous Raman spectroscopy of blood serum samples to distinguish between gastric cancer patients ($n = 29$) and healthy controls ($n = 40$).[30] Using the partial least-squares discriminant analysis (PLS-DA) method, 87.5% of gastric cancer patients and healthy controls were diagnosed correctly.[30] Avram et al. analyzed serum samples collected from patients with gastrointestinal tumors ($n = 53$) and healthy controls ($n = 25$) using SERS, which was acquired with a portable Raman device.[31] The SERS serum spectra displayed changes in the intensity of the bands ascribed to carotenoids and purine metabolites between the cancer and control groups, enabling discrimination between the cancer and control groups using PCA-QDA with a 76.92% accuracy.[31] The accuracy was improved to 83.33% when the SERS spectra were combined with C-reactive protein levels, neutrophil counts, platelet counts, and hemoglobin levels inflammatory markers. This study has shed light on the potential of SERS-based biofluid utilizing a portable Raman device for the point-of-care diagnosis of gastrointestinal cancer.[31] Lin et al. developed a new approach to detect a modified nucleoside biomarker for the diagnosis of gastric and breast cancers.[32] In this approach, the modified nucleoside was separated from the patient's urine and purified using affinity chromatography. SERS spectra were acquired for the modified nucleosides collected from gastric cancer patients ($n = 50$), breast cancer patients ($n = 43$), and healthy controls ($n = 48$). The diagnostic sensitivity for identifying gastric cancer vs normal, breast cancer vs normal, and gastric cancer vs breast cancer in a different binary classification model based on PCA-LDA was 84.0%, 76.7%, and 82.0%, respectively, and the corresponding diagnostic specificities for each group were 95.8%, 87.5%, and 90.7%, respectively.[32]

Breast Cancer. SERS and spontaneous Raman spectroscopy were performed using serum samples collected from breast cancer patients ($n = 17$) and healthy controls ($n = 12$) for the classification of different stages of breast cancer. SERS bands attributed to DNA, proteins, and lipids were detected only in the spectra of patients at different stages of breast cancer in comparison with healthy controls.[33] The PLS-DA model based on SERS data provided sensitivity and specificity of 90% and 98.4%, respectively, for the classification of different stages of breast cancer, which were higher than those based on spontaneous Raman spectra, which were 88.2% and 97.7%, respectively.[33] Lin et al. also analyzed the SERS spectra of serum samples collected from breast cancer patients ($n = 30$) with pre- and postsurgery and healthy controls ($n = 30$).[34] The PCA-LDA model of SERS spectra yielded accuracies of 95% and 100% for presurgery versus postsurgery and presurgery
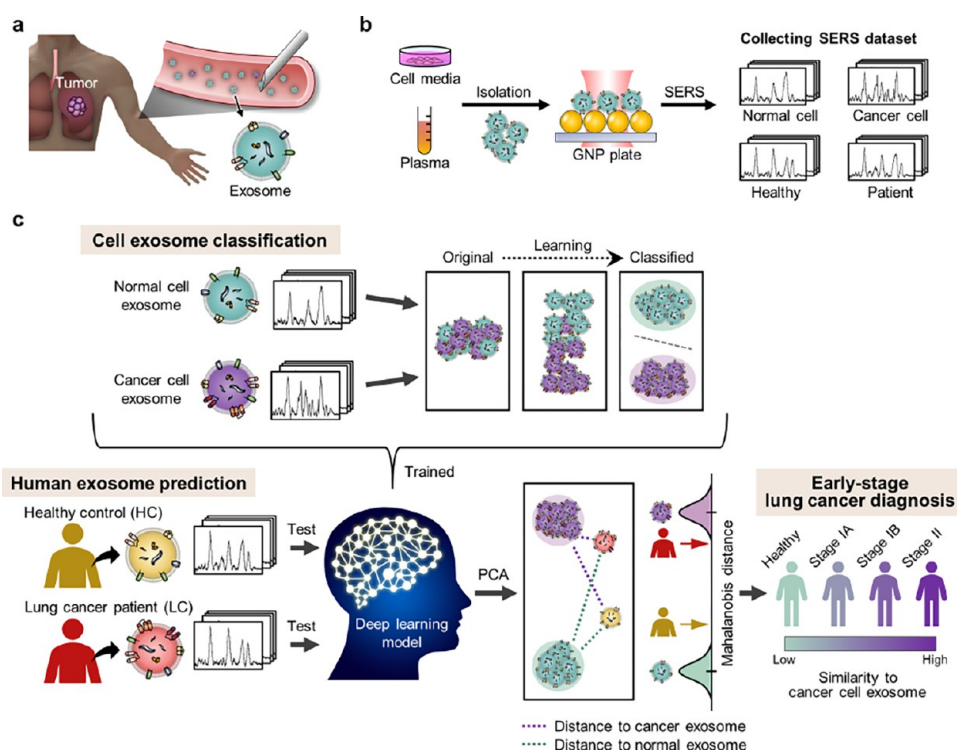
Figure 1. Schematic illustration of deep learning-based circulating exosome analysis for lung cancer diagnosis. (a) Circulation of lung cancer tumor exosomes in the bloodstream. (b) Collection of spectroscopic data of exosomes using surface-enhanced Raman spectroscopy (SERS). (c) Overview of deep learning-based cell exosome classification and lung cancer diagnosis using exosomal SERS signal patterns. Reproduced from Shin, H.; Oh, S.; Hong, S.; Kang, M.; Kang, D.; Ji, Y.-g.; Choi, B. H.; Kang, K.-W.; Jeong, H.; Park, Y.; Hong, S.; Kim, H. K.; Choi, Y. *ACS Nano* **2020**, *14*, 5435−5444 (ref 39). Copyright 2020 American Chemical Society.

versus normal groups, respectively. This study provides a suitable method based on blood analysis for surgery evaluation in addition to breast cancer screening.[34] In another study, SERS spectra were acquired for serum samples collected from healthy volunteers ($n = 39$) and from patients diagnosed with breast ($n = 42$), colorectal ($n = 109$), lung ($n = 33$), oral ($n = 17$), and ovarian cancer ($n = 13$). The PCA-LDA of the SERS spectra was used to differentiate between cancer patients and controls with 98% sensitivity and 91% specificity.[35] In different binary classification models, each cancer type was compared to the controls, and cancer samples were classified with an accuracy of 88%, 86%, 80%, 76%, and 59% for oral, colorectal, ovarian, breast, and lung cancers, respectively.[35] These findings promote the prospective of SERS for the screening for different cancer types.

Furthermore, Kim et al. demonstrated the potential of human tears for detecting breast cancer using a portable Raman spectrometer with a Au/HCP-PS (hexagonal-close-packed polystyrene) monolayer SERS biosensor.[36] The leave-one-out-cross-validation (LOOCV)-assisted PC-LDA yielded a classification accuracy of 96%. However, this study was applied to a small number of tear samples collected from breast cancer patients ($n = 5$) and healthy controls ($n = 5$), and further investigation using a large cohort is necessary to show the potential of this approach.[36] Further, Moisoiu et al. performed SERS spectral measurements of unprocessed urine collected from breast cancer patients ($n = 53$) and healthy controls.[37] PCA-LDA distinguished between the SERS spectra of breast cancer patients and healthy controls with 81% sensitivity, 95% specificity, and 88% overall accuracy.[37]

Lung Cancer. For the screening and staging of lung adenocarcinoma, SERS measurements were acquired for serum samples from healthy controls ($n = 82$) and patients with adenocarcinoma ($n = 108$). A classification model, orthogonal partial least-squares discriminant analysis (OPLS-DA), produced a specificity and sensitivity of 97.6% and 98.1%, respectively, using leave-one-patient-out cross-validation (LO-POCV). The staging of lung adenocarcinoma was also accomplished, with overall accuracies of 84.3−86.5% for different stages.[38]

Furthermore, early stage lung cancer diagnosis with high accuracy was achieved utilizing an approach based on deep learning of SERS data of human plasma-derived exosomes (Figure 1). First, a model based on deep learning was trained with SERS spectra of exosomes derived from normal and lung cancer cell lines, and binary classification of cell types with 95% accuracy was achieved. In addition, the plasma exosomes from 90.7% of lung cancer patients ($n = 43$) are similar to lung cancer cell exosomes in comparison with healthy controls ($n = 20$). These findings show the potential of this approach for the early stage diagnosis of lung cancer.[39] SERS was also used to differentiate between malignant pleural effusion ($n = 51$) and benign pleural effusion ($n = 32$) with sensitivity and specificity of 92.2% and 93.8%, respectively, using OPLS-DA.[40]

Interestingly, Ke et al. conducted the first meta-analysis of diagnostic studies to investigate the diagnostic value of Raman spectroscopy in lung cancer.[41] Spontaneous Raman spectroscopy of lung cancer samples, including serum, saliva, and tissues covering 14 studies, provided a total pooled sensitivity and specificity of 92% and 94%, respectively. The pooled sensitivity of 88% and specificity of 87% were achieved in the

case of employing serum samples, while those using saliva samples were 91% and 95%, respectively. It should be mentioned that when serum and saliva samples were applied, the accuracy of spontaneous Raman spectroscopy was detailed in four studies. Thus, it is necessary to conduct large-scale diagnostic studies to validate these findings.

Bladder Cancer. Hu et al. performed SERS measurements of urine supernatant and urine sediment from patients diagnosed with bladder cancer ($n = 161$) and healthy controls ($n = 87$), providing information on both metabolomics and cytology to detect bladder cancer and predict tumor grading.[42] PCA-LDA of SERS spectra predicted the sensitivity and specificity for high-grade tumors to be 100% and 98.85%, respectively, and 97.53% and 90.80%, respectively, in the case of low-grade tumors.[42] In addition, Chen et al. compared the SERS spectra of blood serum samples collected from nonmuscle-invasive bladder cancer (NMIBC), muscle-invasive bladder cancer (MIBC), and healthy controls, and an accuracy of 93.3% was achieved using PLS-LDA. Using two different binary classification models produced diagnostic accuracy of 97.8% and 93.2% for healthy versus bladder cancer groups and for NMIBC versus MIBC groups, respectively.[43]

Esophageal Cancer. Maitra et al. applied a combination of spontaneous Raman spectroscopy and genetic algorithm quadratic discriminant analysis (GA-QDA) on biofluids (plasma, serum, saliva, and urine) to distinguish different stages of esophageal adenocarcinoma.[44] Classification accuracy of 100% was achieved for all esophageal stages (normal/squamous epithelium, inflammatory, Barrett's, low-grade dysplasia (LGD), high-grade dysplasia (HGD), and esophageal adenocarcinoma (OAC)) using saliva and urine samples, while the accuracy of >90% was obtained using plasma and serum samples.

Oral Cancer. Sahu et al. acquired spontaneous Raman measurements of exfoliated cells collected from a tumor ($n = 16$), contralateral normal mucosa ($n = 16$) of oral cancer patients, and healthy tobacco smokers ($n = 20$).[45] A classification based on PCA-LDA, including the three classes, produced an accuracy of 70% using LOOCV. In another study using exfoliated cells, PCA-LDA of spontaneous Raman or FTIR spectra of saliva collected from healthy donors ($n = 13$) and pathologically confirmed oral ($n = 11$) and oropharyngeal ($n = 8$) cancer patients ($n = 19$) resulted in an accuracy of 90% and 82%, respectively.[46] The accuracy based on the Raman spectra was better than that obtained in a similar study using saliva collected from normal ($n = 13$), precancerous ($n = 13$), and cancerous ($n = 10$) conditions.[47]

Thyroid Cancer. A combination of line-scan Raman spectral imaging, PCA, and LDA was employed to classify single cells from fine-needle aspiration (FNA) biopsies of a benign thyroid ($n = 127$) and a classic variant of papillary carcinoma ($n = 121$). Spectral changes were observed between benign and papillary carcinoma cells, reflecting molecular changes in phenylalanine, tryptophan, proteins, lipids, and nucleic acids, leading to cell classification with a high diagnostic accuracy of 97%.[48] Besides, the results of cells from follicular adenoma ($n = 20$), follicular carcinoma ($n = 25$), and follicular variant of papillary carcinoma ($n = 18$) nodules propose the eventuality of spontaneous Raman spectral imaging for further subtyping of thyroid cancer. Xia et al. assessed the probability of applying SERS of blood serum to differentiate between benign ($n = 19$) and malignant thyroid ($n = 22$) nodules as well as healthy volunteers ($n = 22$).[49] The PLS-LDA model based on SERS

spectra produced an accuracy, sensitivity, and specificity of 93.65%, 92.68%, and 95.45%, respectively, for differentiating between healthy and thyroid nodular groups, while those of 82.93%, 81.82%, and 84.21% were achieved for benign versus malignant groups.[49] However, Liang et al. performed SERS measurements of blood plasma from patients with a benign thyroid tumor ($n = 32$) and thyroid cancer ($n = 70$) after utilizing filter membranes to remove macromolecular proteins in blood plasma. PCA-LDA and Lasso-PLS-DA models of SERS spectra yielded 84.3% and 90.2% discrimination accuracy, respectively.[50] These results show the potential of SERS-based blood analysis for the detection of thyroid tumors.

Ovarian Cancer. Giamougiannis et al. compared the spontaneous Raman spectra of blood plasma, serum, and ascetic fluid collected from patients diagnosed with ovarian cancer ($n = 18$) and benign controls ($n = 20$). Different discrimination models, including PCA-LDA, PCA-QDA, PCA-SVM, and PLS-DA, were used, and ascetic fluid produced the best class separation with accuracies, sensitivities, and specificities above 80%, while 60−73% was obtained in the case of plasma or serum. Changes in the Raman bands attributed to collagen are the reason to distinguish ovarian cancer samples.[51] Besides, SERS has been used to detect haptoglobin, a potential diagnostic biomarker for epithelial ovarian cancer, in ovarian cyst fluids collected from benign cysts ($n = 57$) and malignant cysts ($n = 57$). SERS detection of haptoglobin produced sensitivity and specificity of 94% and 91%, respectively, in comparison with histology, showing the potential of SERS-based diagnostic assays for use in an intraoperative setting.[52]

Neurodegenerative Diseases. Diagnosis of neurodegenerative diseases is still problematic, and disease-specific biomarkers remain elusive. Therefore, the search for biomarkers for neurodegenerative diseases has continued to use various novel tools. Ralbovsky et al. examined saliva from patients with Alzheimer's disease (AD; $n = 39$), mild cognitive impairment, and normative using spontaneous Raman hyperspectroscopy.[53] Genetic algorithm (GA) and ANNs were applied to distinguish between the three classes with an accuracy of 99−100%, using either internal or blind external validation.[53] CSF was also studied by the same research group to diagnose AD. Spontaneous Raman spectra were acquired from CSF samples collected from patients diagnosed with AD ($n = 21$) and healthy controls ($n = 16$). The differentiation between these two classes was achieved with 84% sensitivity and specificity using ANNs and support vector machine discriminant analysis (SVM-DA).[54] SERS measurements were performed using blood serum from patients with AD ($n = 10$) and healthy controls ($n = 11$). Using LOOCV, PCA and LDA provided a diagnostic accuracy of 83%, precision of 86%, and specificity of 86%. By comparing the SERS spectra with those obtained from MRI, a correlation between the SERS spectra and hippocampus degeneration was demonstrated, implying the potential of the SERS method for monitoring AD progression.[55] Besides, blood serum samples from AD patients ($n = 20$), healthy controls ($n = 19$), and patients with other neurodegenerative dementias (OD, $n = 18$) were analyzed using SERS coupled with ANNs. In a binary classification model, ANNs achieved a diagnostic accuracy of 96% to differentiate between AD patients and healthy controls, while 98% accuracy was obtained for detecting AD, healthy controls, and OD in a tertiary model.[56] Furthermore, Zhang et al. applied SERS to investigate amyotrophic lateral sclerosis

(ALS) using blood plasma collected from sporadic ALS patients ($n = 138$), including short-duration group (≤ 3 years, $n = 62$) and long-duration group (>3 years, $n = 76$).[57] SERS results revealed significant differences between these two groups, which could be differentiated with an AUC of 0.972.[57]

Diabetes. For diabetes patients, self-monitoring of blood glucose (SMBG) levels has been advised a minimum of four times per day. However, the popular devices employed to monitor blood glucose depend on invasive protocols to provide blood for examination (testing capillary blood), uncomfortable for patients and sometimes resulting in poor compliance.[58] Furthermore, continuous glucose monitoring (CGM) systems with indwelling sensors measure the glucose levels in the subcutaneous interstitial fluid for 6–14 days. This technology provides increased accuracy and simplified handling of CGM systems, leading to the partial replacement of SMBG systems. However, CGM systems are quite invasive and can lead to some complications.[59] Until now, noninvasive technologies are not yet used in a clinical routine. Among them, spontaneous Raman spectroscopy showed great potential for diabetes diagnosis because of its glucose specificity.[60] Based on a low-cost poly(methyl methacrylate) microneedle array, a novel SERS sensor was developed for the *in vivo* intradermal detection of glucose. For the *in vivo* quantification of glucose, the sensor was examined in a type I diabetes mouse model.[61] The results revealed that the sensor detected glucose in the interstitial fluid within a few minutes and maintaining its structural integrity, in addition to its minimal invasiveness of the skin.[61] Kang et al. directly observed Raman bands, which are specific to glucose *in vivo* skin.[60] In the three live swine glucose clamping experiments, the intensity of the Raman bands changed proportionally to the concentrations of the reference glucose. These results may end the debate on whether spontaneous Raman spectroscopy can directly detect *in vivo* glucose Raman bands.[60] A table-top confocal Raman spectrometer was developed by Lundsgaard-Nielsen et al. and applied at home for patients ($n = 35$) with diabetes.[62] It noninvasively monitors the interstitial glucose in the skin and is operated for 60 days, unsupervised, and the results demonstrated the first successful application of a noninvasive glucose monitor at home.[62] Up to 25 days at home and in an in-clinic setting, Pleus et al. tested this developed prototype, GlucoBeam device, to monitor noninvasively glucose in patients ($n = 15$) with type I diabetes.[63] In this proof-of-concept study, calibration models were established and independent validation data, including a blinded in-clinic day with glucose excursion, were collected. The results revealed accuracy comparable to that of early generation CGM systems.[63] In another study, skin glycated proteins were identified using Raman and fluorescence methods for non-invasive screening of diabetes.[64]

Malaria. Malaria, a widespread mosquito-borne disease, is one of the deadliest human diseases. Malaria affects more than 500 million people every year.[65] Early diagnosis of malaria is crucial to reduce mortality rates. Spontaneous Raman spectroscopy has been used to investigate *Plasmodium*-infected and uninfected erythrocytes. The diagnosis of malaria is based on the identification of *Plasmodium* in the blood. Raman spectra of blood serum of dengue-infected ($n = 39$) and malaria-infected ($n = 37$) donors were compared to those of healthy controls ($n = 54$). PCA-LDA provided an average accuracy of ~89% for differentiation between malaria, dengue, and healthy control classes.[66] The spontaneous Raman results

were complemented by mass spectroscopy of serum samples, where several metabolites referred to Raman peaks, were also recognized by mass spectrometry.[67] Ngo et al. established a nanophotonic-based assay for point-of-care diagnostics of malaria suitable for low and middle-income countries. The method directly detects *P. falciparum* RNA in red blood cell lysates using SERS. This method can detect low concentrations with a detection limit of up to 200 fM.[68] Besides, Wang et al. established a rapid antibody-free diagnostic method of malaria infection with *P. falciparum* ($n = 5$) and *P. vivax* ($n = 10$) in blood lysate using SERS.[69] In this study, the Raman bands at 1370 cm^{-1}, 1570 cm^{-1}, and 1627 cm^{-1} were employed to identify positive malaria in comparison with healthy control samples ($n = 10$). The detection limit of this method is 10^{-5} dilution, corresponding to the concentration of parasitized blood cells of 100/mL.[69] However, the number of measured samples is small and measurements of large cohorts are required to validate these results. Mhlanga et al. fabricated sandwich biosensing-based SERS probes to detect and quantify malaria. To capture *P. falciparum* malaria antigen, lactate dehydrogenase (LDH) malaria antibody (mAb) was immobilized on a SERS substrate. The detection hybrid, Ag plasmonic metals labeled with a SERS tag and conjugated to a second LDH mAb were hybridized on the captured antigen.[70] It binds the antigen, and the sandwich is interpreted using SERS, which proves the pfLDH malaria antigen through the SERS tag. SERS spectra were observed even at 1 parasite/μL, implying a higher sensitivity of the fabricated probes.[70]

Bacterial and Viral Infections. Raman spectroscopy is an attractive bioanalytical tool for clinical translation in microbiology laboratories. This is because the classification of pathogenic bacteria can be assisted via the profiling of prokaryotic cells. In microbiology, several methods are applied to detect and identify pathogenic bacteria, such as serology, immunological and molecular testing, microbial cultures, and microscopy. However, there are several shortcomings accompanied by these methods, including being time-consuming and labor-intensive, cross-reactivity, poor specificity, and high cost, especially for immunological and molecular techniques.[71,72] Therefore, there is an unmet demand for fast and high-throughput tools to identify pathogenic bacteria with high accuracy, enabling therapeutic intervention at a suitable time.

Sepsis is a systemic inflammatory response syndrome induced by infection and is a life-threatening medical emergency. Most cases (70%) occurred due to bacterial infections compared to viral (20%) and fungal (10%) infections. However, not all cases need to result in sepsis. Early stage diagnosis and therapy can decrease the mortality rate of patients with sepsis. In sepsis diagnosis, identification of the pathogen is not the only important step, and identifying biomarker concentrations, such as lactate and C-reactive protein, are important in stratifying patients and determining clinical actions.[73] The current gold standard for detecting infection in the blood is positive blood culture. However, it has several limitations, including the high volume of blood required and it may take up to several days for pathogen detection and identification, while the host's condition worsens.[74] Label-free Raman spectroscopy can overcome these shortcomings by implementing a fast and cheap tool for blood analysis with little sample preparation.[75] For instance, Wang et al. established an assay based on SERS for fast and quantitative detection of interleukin 6 (IL-6).[76] In the case of infection stimulation, IL-6 is an appropriate predictor of

severe sepsis.[77] Serum samples (n = 57) were measured using SERS and simultaneously detected through the clinically used chemiluminescence, and the results revealed a good correlation (R^2 = 0.9793, P < 0.01). The developed assay presents a novel reference for the detection of sepsis biomarkers.[76]

Lee et al. constructed peptidoglycan-binding protein (PBPMs) and used it to capture Gram-positive bacteria with high efficiency.[78] The quantitative analysis of the captured bacteria was accomplished by SERS within 30 min and detected *Staphyloccocus aureus* associated with sepsis at a low concentration of 10 colony forming units (cfu)/mL in human plasma.[78] In another study, De Plano et al. chose phage clones that explicitly bind the surface of *Staphyloccocus aureus*, *Pseudomonas aeruginosa*, and *Escherichia coli* from M13 phage display libraries and functionalized them with commercial magnetic beads.[79] These were used to capture and concentrate the bacteria involved in sepsis from the blood, which was detected using spontaneous Raman microspectroscopy with a detection limit of 10 cfu in 7 mL of blood.[79]

The antibiotic susceptibility test (AST) is crucial for the diagnosis of bacterial infections, including sepsis. Timely effective antibiotic use to treat infections is critical for patients' lives. AST normally needs 2−5 days for sample culture, antibiotic treatment, and collection of results. Chang et al. developed a microfluidic system integrating membrane filtration and a SERS substrate to perform on-chip bacterial enrichment and *in situ* SERS measurements to detect bacterial metabolic activity.[80] The bacterial concentration detection limit by SERS is 103 cfu/mL, which is much lower than that detected utilizing the centrifugation−purification procedure, leading to a decrease in bacterial culture time.[80] Han et al. also established a protocol that can obtain AST results based on SERS of blood culture samples within 4 h.[81] Furthermore, Yi et al. developed an AST-based fast Raman spectroscopy (FRAST) that detects single bacterial metabolic activity in the presence of antibiotics.[82] FRAST was applied to urinary infectious samples (n = 9) and sepsis samples (n = 3). FAST results were in agreement with both conventional AST and matrix-assisted laser desorption ionization-time-of-flight (MALDI-TOF) identification.[82] This approach should be applied to large cohort samples in further studies. Spontaneous Raman- or SERS-based AST present rapid and reliable susceptibility tests, which may be suitable for clinical practice.

Verma et al. explored the potential of spontaneous Raman spectroscopy to identify sepsis biomarkers employing different mouse models of inflammation. The sepsis-induced mouse model displayed hemolysis, as shown for the first time by the Raman bands characteristic of the hemoglobin porphyrin ring.[83] Furthermore, Yarbakht et al. employed a combination of nonlinear imaging modalities, including CARS, TPEF, and SHG, to examine the consequences of early septic liver injury in a murine model.[84] An excellent differentiation between liver sections from septic mice and sham-treated mice was achieved using CARS (AUC = 0.93) and TPEF (AUC = 0.83) imaging, in contrast to SHG (AUC = 0.49). The results also suggest alterations in hepatic lipid distribution and metabolism during liver injury and show the potential of label-free CARS and TPEF imaging to explore septic liver damage.[84]

Furthermore, SERS and PLS-DA were applied to detect 215 methicillin-resistant *Staphylococcus aureus* (MRSA) and 52 methicillin-sensitive *Staphylococcus aureus* (MSSA) isolates with an accuracy of 100%. This study highlights the prospect of SERS for investigating antibiotic resistance.[85] Furthermore,

Hernández-Cedillo et al. monitored the level of sialic acid in the saliva of patients with periodontal disease (n = 33), gingivitis (n = 30), and controls (n = 30) using SERS.[86] Sialic acid concentrations were determined for control, gingivitis, and periodontitis patients to be 5.98, 7.32, and 17.12 mg/dL, respectively. These results indicate the feasibility of utilizing SERS for the diagnosis of bacteria-causing oral diseases.[86]

Spontaneous Raman spectroscopy was used to investigate viral infections, such as hepatitis B (HBV) and hepatitis C (HCV). Tong et al. examined blood serum samples from patients infected with HBV (n = 500) and non-HBV patients (n = 500).[87] PCA and SVM were used for modeling and prediction, and the two groups were verified using a double-blind verification method. In the first group, a sensitivity of 87% and specificity of 92% were obtained, while a sensitivity of 80% and specificity of 79% were achieved in the second group. These results show the potential of spontaneous Raman spectroscopy for HBV detection.[87] Ditta et al. also examined blood plasma from HCV-infected patients (n = 11) and healthy controls (n = 10).[88] The HCV-infected patients were divided into three groups based on viral load values: low, medium, and high viral loads. The Raman results were analyzed using PCA and revealed spectral differences between HCV-infected and noninfected groups, reflecting the development of biochemical changes upon HCV infection.[88] Further studies using large cohorts are required to validate these results since a small cohort was measured.

To determine the ability of spontaneous Raman spectroscopy to differentiate between two infectious diseases with symptom similarities, such as typhoid and dengue, Raman spectra of blood serum were recorded from *Salmonella typhi*-infected (n = 20) and dengue-virus infected (n = 22) patients.[89] PCA with LDA was applied to differentiate between the two sets of data, demonstrating the prospective of spontaneous Raman spectroscopy to classify two different pathological conditions with similar symptoms.

In December 2019, the first case of SARS-CoV-2 infection was detected in China. After that, the COVID-19 epidemic has quickly grown worldwide, and people have suffered severe health fears and socio-economic burdens. The main obstacles in current diagnostics for COVID-19 are the need for experienced staff and costly and time-consuming methods. Since the outbreak of COVID-19, tremendous efforts were made to establish novel and fast diagnosis methods with high accuracy to identify SARS-CoV-2 that would be distributed globally to control the pandemic.[90] For example, Carlomagno et al. described a spontaneous Raman approach based on the analysis of saliva to discriminate between patients affected by COVID-19 (COV+; n = 30), patients with a past COVID-19 infection (COV−; n = 38), and controls (n = 33). The results revealed spectral differences in saliva biochemical composition of the three groups, enabling discrimination of the spectra collected from the three groups with accuracy greater than 87.6% using LDA. Using the deep learning CNN approach, an accuracy of 89−92% was achieved at the patient level.[91] Yin et al. acquired spontaneous Raman spectra of serum samples collected from patients diagnosed with COVID-19 (n = 63), suspected cases (n = 59), and healthy controls (n = 55).[92] The SVM model provided binary classifications between the COVID-19 cases and the suspected cases, COVID-19 and the healthy controls, and suspected cases and healthy controls, with an accuracy of 87%, 90%, and 68%, respectively. For independent test data sets, five asymptomatic and five
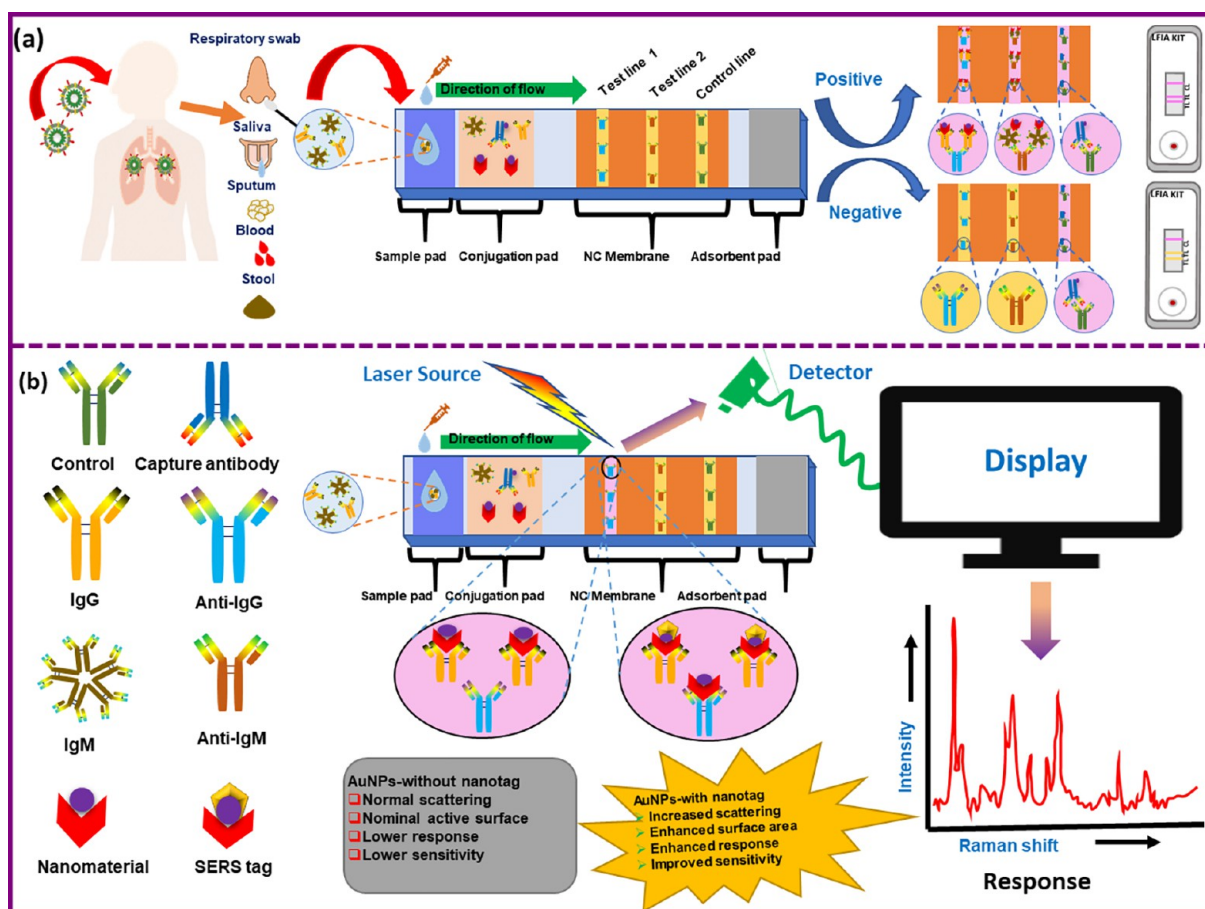
Figure 2. Schematic representation of the fabrication and working principle of (A) conventional LFIA and (B) SERS-based LFIA for detection of SARS-CoV-2. Reproduced from Yadav, S.; Sadique, M. A.; Ranjan, P.; Kumar, N.; Singhal, A.; Srivastava, A. K.; Khan, R. *ACS Appl. Bio. Mater.* **2021**, *4*, 2974−2995 (ref 95). Copyright 2021 American Chemical Society.

symptomatic COVID-19 patients, five suspected patients, and five healthy controls were measured for external validation. With the SVM model, classification was achieved with an overall accuracy of 90% for all classes.[92]

Furthermore, some developments were made for COVID-19 identification via strip-based tests. For instance, lateral flow immunoassay (LFIA) and point-of-care testing (POCT) is considered one of the most prevalent methods. This is because it is simple, flexible, fast, and inexpensive, and it can be applied in several public places because there is no need for skilled personnel.[93,94] LFIA approach (Figure 2) based on serological testing of anti-SARS-CoV-2 IgM/IgG can be utilized alone or joining other methods, including the SERS method to obtain better results.[95] The SERS-LFIA sensor was examined on serum samples collected from patients diagnosed with COVID-19 ($n = 19$) and healthy controls ($n = 49$), and the results demonstrated the clinical feasibility of the assay and high accuracy was obtained for the detection of COVID-19 patients.[96]

Raman Spectroscopy for Histopathology. Histopathology is the diagnosis of diseases, such as cancers, and it involves the visual examination of stained tissue sections using light microscopy. It is performed on tissue sections preoperatively, intraoperatively, or postoperatively, and it monitors the morphological changes that take place upon disease progression.[97] The staining of the tissue sections is performed using hematoxylin/eosin (H&E), which allows visualization of

basic proteins of the histones and cellular cytoplasm.[98] Histopathology depends on the pathologist's expertise and suffers from an inter-/intraobserver dilemma. In addition, it is time-consuming and needs a laboratory; therefore, it is unsuitable in the operating theater where a quick decision must be made. Real-time assessment of resected tissues and correct pathological diagnosis are required for intraoperative applications. To decrease the interobserver variability of histopathology, efforts have been dedicated to quantifying image information and presenting it to physicians as computer-aided diagnostic tools, which are generally denoted as digital pathology.[99] However, such results are based on external staining that provides only morphological information with low inherent differentiation between healthy and disease-specific structures in tissue rather than molecular information. In addition to H&E staining, immunohistochemistry (IHC) is used, in which single specific molecular targets act as disease biomarkers to increase the quantitative information extracted from histological samples. Although this approach can monitor the variations in biochemical composition as the existence of specific diagnostic biomarker molecules to differentiate between healthy and diseased tissues, it has significant limitations.[100]

In the last few decades, vibrational spectroscopic methods have been developed that can monitor the spectral bands of tissue components, and the vibrational spectrum in this case reflects a molecular "fingerprint". This molecular "fingerprint"
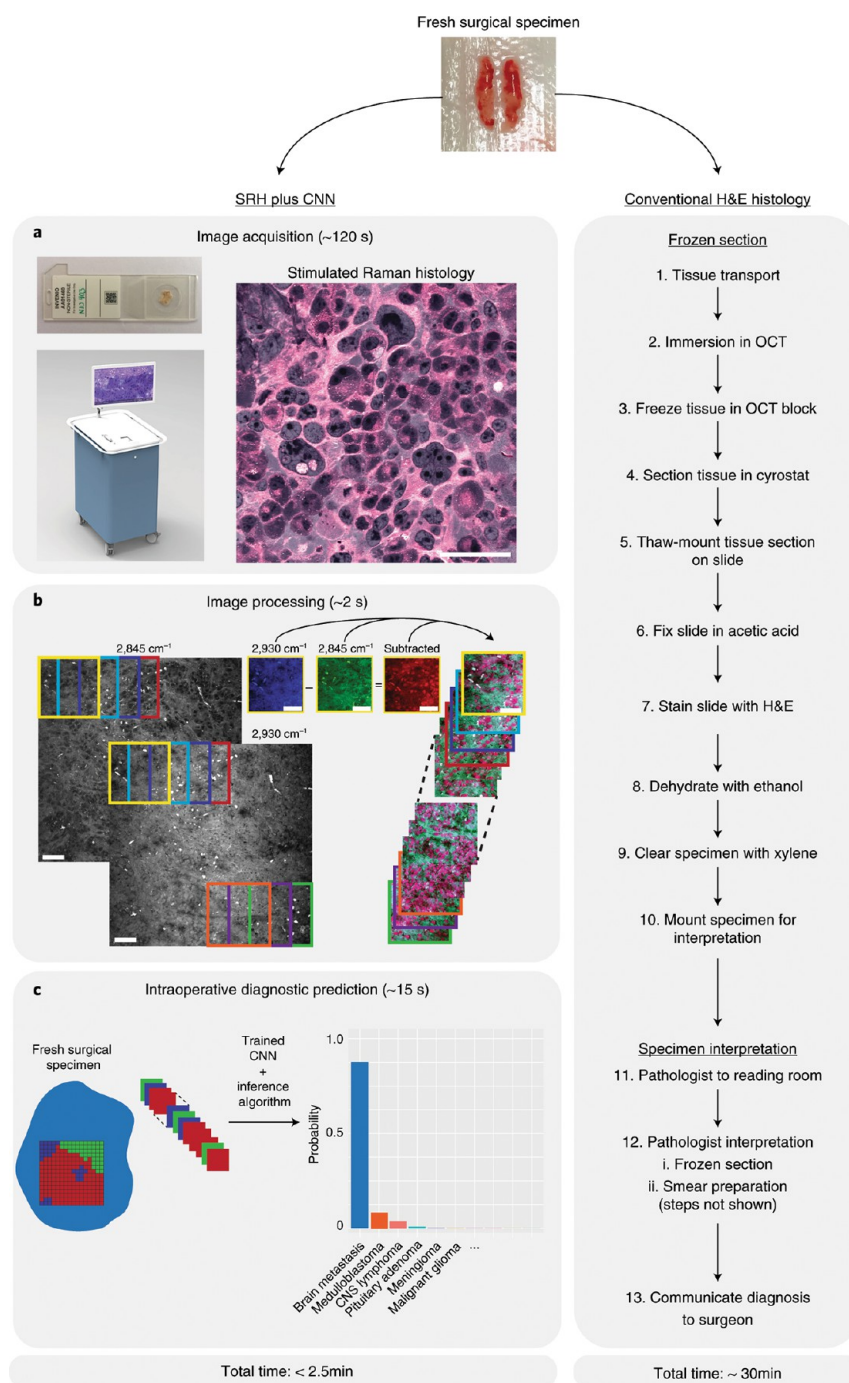
Figure 3. Intraoperative diagnostic pipeline using SRH and deep learning. The intraoperative workflows for both conventional H&E staining histology and SRH plus CNNs are shown in parallel. (a) Freshly excised specimens are loaded directly into an SRH imager for image acquisition. Operation of the SRH imager is performed by a single user, who loads tissue into a carrier and interacts with a simple touch-screen interface to initiate imaging. Images are sequentially acquired at two Raman shifts, 2845 and 2930 cm^{-1}, as strips. After strip stitching, the two image channels are registered, and virtual H&E provides SRH mosaics for an intraoperative review by surgeons and pathologists. (b) Image processing starts by using a dense sliding window algorithm with valid padding over the 2845 and 2930 cm^{-1} images concurrently. Registered 2845 and 2930 cm^{-1} image patches are subtracted pixel wise to generate a third image channel (2930 cm^{-1} to 2845 cm^{-1}) that highlights nuclear contrast and cellular density. Each image channel is postprocessed to enhance image contrast and concatenated to produce a single three-channel RGB image for CNN input. (c) To provide an intraoperative prediction of brain tumor diagnosis, each patch undergoes a feedforward pass through the trained CNN and takes approximately 15 s using a single graphics processing unit (GPU) for the 1 × 1 mm^2 SRH image. Scale bar, 50 μm. Reprinted by permission from Macmillan Publishers Ltd.: NATURE Medicine, Hollon, N. et al., *Nature Medicine* **2020**, *26*, 52−58 (ref 108). Copyright 2020.

represents the integral signature of the proteome, genome, lipidome, and metabolome of the measured tissue instead of detecting specific markers as in IHC. Such methods can perform a label-free digital pathology. Here, we review recent applications of Raman methods in histopathology and consider their potential in the future.

Cancer Diagnostics. Bladder Cancer. Cordero et al. investigated tissue heterogeneity and grading of bladder

tumors ($n = 28$) using a fiber probe-based spontaneous Raman imaging instrument.[101] Two-step classification models based on PLS-LDA were built, and a sensitivity of 92% and specificity of 93% were predicted in the first-level model to differentiate between tumor and nontumor biopsies. In the second step, a sensitivity of 85% and a specificity of 83% were obtained to discriminate between high-grade and low-grade bladder tumors.[101] A combination of optical coherence tomography (OCT) and spontaneous Raman imaging-based fiber probe was developed by Placzek et al. for the detection and grading of 119 biopsies collected from NMIBC patients ($n = 44$).[102] On the one hand, the PLS-LDA classification model was built and provided a sensitivity and specificity of 78% and 69%, respectively, for the detection of NMIBC by OCT. On the other hand, spontaneous Raman imaging provides a sensitivity and specificity of 81% and 68%, respectively, for distinguishing between low- and high-grade tissues. The results suggest that a combined OCT and Raman fiber-probe imaging approach has a prospective as a label-free approach for bladder cancer diagnostics.[102]

Breast Cancer. Spontaneous Raman spectroscopy was used to measure different tissue sections from patients ($n = 20$) with benign breast lesions (fibrocystic, fibroadenoma, intraductal papilloma) and breast cancer (invasive ductal carcinoma and lobular carcinoma). Different models, such as PCA-LDA, PCA-QDA, and PLSDA differentiated between normal and cancer patients with sensitivity and specificity higher than 80%, while sensitivity and specificity higher than 90% were achieved using RBF SVM models.[103] Interestingly, Koya et al. utilized spontaneous Raman spectroscopy coupled with CNNs to discriminate between normal ($n = 44$) and cancerous ($n = 44$) basal and luminal breast tissue with sensitivity and specificity of 88.9% and 90.8%, respectively. The Raman images display the boundaries between normal adipose tissues, connective tissues, and tumors. Thus, Raman imaging can serve as a laboratory tool to aid the intraoperative tissue assessment.[104] Furthermore, autofluorescence imaging and spontaneous Raman spectroscopy were performed on breast tissue sections ($n = 14$) and coupled with deep learning algorithms with PLS to increase the diagnostic accuracy of breast cancer. By using autofluorescence images, the discriminant accuracy for the validation and test sets was 89.5% and 88.61%, respectively, while it measured 97−100% and 95.33−98.67%, respectively, using Raman spectra.[105] Ali et al. applied nonlinear multimodal imaging techniques, including CARS, TPEF, and SHG, in combination with deep convolutional neural networks (DCNNs) for automatic detection of breast cancer ($n = 21$).[106] The DCNN ResNet50 was used either as a feature extractor or fine-tuned as a classification model. Using the fine-tuned ResNet50 network and LOPOCV produced the best results for breast cancer detection with a mean sensitivity of 86.23% and mean specificity of 91.31%.[106]

Colon Cancer. Sarri et al. reported SRS and SHG imaging of healthy, precancerous, and cancerous colon and pancreas tissue sections of unprocessed human surgical specimens.[107] The biochemical and collagen information provided by SRS and SHG, respectively, were used to mimic conventional histopathology (H&E).[107] The results showed great agreement among the SRS/SHG and H&E images acquired from the same patient. In addition, wavelength-switch SRS and frequency-modulated SRS were implemented in the system to create images across a millimeter field of view with a speed compatible with intraoperative context. Such developments pave the way for near real-time and label-free GI histology in an intraoperative setting.[107]

Brain Cancer. Two-color SRS imaging is applied for label-free histopathology and is designated stimulated Raman histology (SRH), which monitors the lipid and protein distribution by acquiring imaging at 2845 and 2930 cm^{-1}, respectively. Remarkable SRH images were obtained and were similar to those of H&E staining. For instance, Hollon et al. performed a nearly real-time intraoperative brain tumor diagnostic approach at the bedside using SRH and DCNNs (Figure 3).[108] In a multicenter study ($n = 278$), CNNs were trained on over 2.5 million SRS images measured at 2845 and 2930 cm^{-1}, predicting brain tumors with an overall accuracy of 94.6% at 150 s faster than conventional methods.[108] In another study, Eichberg et al. performed SRH imaging of tissue sections resected from the brain, spinal cord, or peripheral nerve tumor or lesions ($n = 82$) in a prospective blinded study for intraoperative pathological consultation.[109] A sensitivity of 97.5% and specificity of 100% were achieved much faster than classical histopathology analysis, suggesting that SRH can be implemented in the workflow of a neurosurgical operating room.[109]

Prostate Cancer. Doherty et al. reported that a combination of digital histopathology and spontaneous Raman imaging may advance the diagnosis of prostate cancer because of incorporating morphological and biochemical information.[110] Using a binary classification model, a sensitivity of 73.8% and a specificity of 88.1% were predicted for the G3/G4 classification, while a sensitivity of 54.1% and specificity of 84.7% were obtained using only digital histopathology.[110]

Head and Neck Cancer. Zhang et al. distinguished between normal ($n = 34$) and laryngeal squamous cell carcinoma ($n = 44$) using SRH imaging at only two wavenumbers (2845 and 2930 cm^{-1}) in addition to SHG imaging.[111] The deep learning-based histopathology model, ResNet34, distinguished neoplastic tissue from healthy tissue sections with 100% accuracy compared to H&E staining.[111] In addition, this approach can recognize tissue neoplasia at the simulated resection margins that seem normal with the visual inspection, showing the potential for delivering a rapid intraoperative diagnosis.[111] Rodner et al. used a new segmentation approach, pixel-wise classification, based on the full CNN of a combination of CARS, TPEF, and SHG images collected from tissue sections of patients with head and neck squamous cell carcinoma (($n = 12$); cavity of the mouth ($n = 1$), oropharynx ($n = 5$), larynx ($n = 4$), and hypopharynx ($n = 2$)).[112] The average recognition rate and an overall recognition rate of the four classes were 88.9% and 86.7%, respectively. Such results should be validated with measurements of a large cohort in future studies.

Skin Cancer. Spontaneous Raman spectral imaging using 830 nm excitation was acquired to discriminate between basal cell carcinoma (BCC) in skin cancer tissue and surrounding normal skin structures ($n = 30$). The results indicated the presence of concentration variations in the nucleus, keratin, collagen, triolein, and ceramide compared to the surrounding healthy skin. A diagnostic model based on such changes, especially the nucleus, was developed and provided a sensitivity and specificity of 90% and 92%, respectively.[113] The same research group also employed a superpixel acquisition approach that is much faster than the traditional point-by-point scanning by reducing the spatial resolution, which is not required for BCC tumor margin assessment ($n = 10$).[114] The results differentiated between tumor and healthy
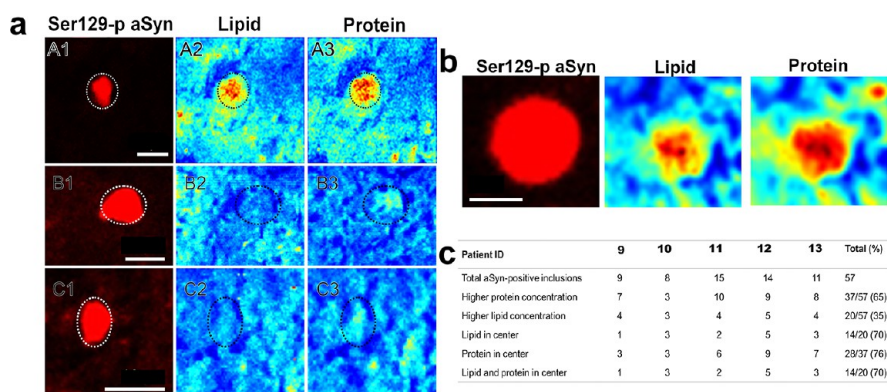
Figure 4. Protein and lipid distribution of nigral LBs using CARS microscopy. (a−c) Various LB compositions as identified by CARS microscopy. Ser129-p aSyn+ inclusions are depicted in the first column, and CARS signal intensities at 2850 and 2930 cm^{-1} highlight their lipid (second column) and protein (third column) distributions, respectively. Low CARS intensities are depicted in blue, whereas high intensities are depicted in red. LBs with different compositions were identified: LBs with high CARS intensities for proteins and lipids compared to the direct environment (top row), with high CARS intensity for proteins but not lipids (middle row), and with low CARS intensity for proteins and lipids (bottom row). (b) Representative image of a LB with high protein and lipid signal centralized in the structure. (c) Numbers and proportions of nigral LBs with high (centralized) lipids or proteins per patient. In total 57 LBs were observed in five PDD patients, of which 37 showed high protein concentrations and 20 showed high lipid concentrations compared to the surrounding tissue. In total, 14 out of 20 with high lipid concentrations displayed lipids mainly in the center, whereas 28 out of 37 displayed mainly proteins in the center. (a) Scale bar = 10 μm and (b) scale bar = 5 μm. Reprinted by permission from Springer Link, Moor, T. E. et al., *Acta Neuropathologica* **2021**, *142*, 423−448 (ref 117). Copyright 2021.

skin with a sensitivity of 82% and specificity of 94% according to the biochemical alterations in nucleus, collagen, keratin, and ceramide. Liu et al. employed 532 nm excitation in the visible region to benefit from the RR enhancement to distinguish between BCC in skin cancer tissue and surrounding normal skin tissue.[115] The PCA-SVM model based on RR spectra produced a sensitivity of 93.0% and specificity of 100% in comparison with the classical histopathology.[115]

Neurodegenerative Diseases. Shahmoradian et al. successfully investigated the composition of Lewy bodies (LBs), the neuropathological hallmark of Parkinson's disease (PD), using several tools, including CARS imaging with subsequent immunofluorescence staining of human brain tissues of PD patients in correlative measurements.[116] LBs showed an increase in the lipid and protein contents in the substantia nigra (SN) and hippocampal CA2 in the same regions that showed a higher αSyn signal in comparison with the surrounding tissue.[116] The summary of the results of several tools including CARS has shown that LBs are comprised of membrane fragments, lipids, mitochondria, and vesicular structures rather than protein fibrils. Moors et al. also reproduced the increased lipid and protein content of LBs using CARS imaging (Figure 4).[117] In addition, CARS imaging revealed substantial heterogeneity in lipid and protein composition of LBs, and the enrichment of proteins and lipids was mainly localized to the central portion of nigral LBs. Central clustering of accumulated lipids and proteins in LBs supports the hypothesis that such components are encapsulated in LBs.[117]

Furthermore, a combination of FTIR and spontaneous Raman spectral imaging, as well as IHC, was performed to investigate different Aβ plaque types in human brain tissue sections collected from post-mortem AD patients. The results showed that the classic cored plaque exhibits aggregated β-sheet protein, as indicated by the shift of the Amide I Raman band to 1665 cm^{-1}.[118] Lochocki et al. employed several techniques, including autofluorescence, spontaneous Raman, and SRS imaging, to study amyloid deposits in AD tissue sections from post-mortem patients.[119] The SRS results

showed that the protein band shifts toward the β-sheet conformation in cored amyloid deposits, similar to the spontaneous Raman results reported by Röhr et al.[118] Besides, the spontaneous Raman results obtained with green laser showed the presence of carotenoids only in the cored amyloid plaque area. This is most likely due to a distinct neuroinflammatory response to the accumulations of misfolded protein.[119] However, the carotenoids were not detected in the Raman spectra when 785 nm excitation was used.[120] Further, Cunha et al. applied a multimodal imaging approach, including spontaneous Raman, CARS, SRS, TPEF, and SHG, to examine the core and halo of Aβ plaques in the hippocampus and cortex of brain tissues from an AD mouse model. A halo biomarker was reported based on unsaturated lipids (band at 3019 cm^{-1}) and two core biomarkers assigned to phenylalanine (1007 cm^{-1}) and amide B (3070 cm^{-1}). The spatial distribution images show the usefulness of the reported three biomarkers in the examination of Aβ plaques.[121]

Raman Spectroscopy for Cytopathology. Cytopathological methods use light microscopy to detect stained cancer cells based only on their morphological characteristics in body fluids, such as swabs or urine specimens. These examinations require a trained pathologist, are time-consuming, and offer limited reproducibility. Cytopathological samples have been used for the noninvasive early detection of cervical and bladder cancers as well as for oral diseases. The cervical screening was performed using the Papanicolau (Pap) test, in which the samples are stained by a combination of dyes. This method relies on a visual inspection of the morphology of the individual cell and identifying precancerous or cancerous cells, making it highly subjective, in addition to a high variation in sensitivity (50−96%).[122−124] The major risk factor for cervical cancer development is the persistent infection with human papillomavirus (HPV).[125] Currently, a Pap test is regularly performed in combination with an HPV test, which has a higher sensitivity. However, it has lower specificity (84%) and is also expensive.[126] The employment of structured cytological screening programs has led to a noticeable decrease in cervical cancer over the past few decades.[127] This has
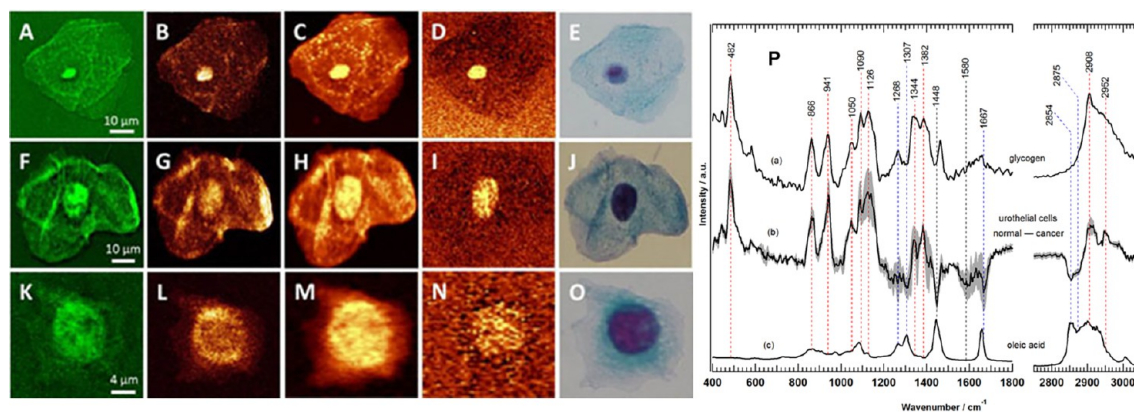
Figure 5. Multimodal imaging techniques of normal (A−E), LSIL (F−J), and HSIL (K−O) cells in Pap smears: (A,F,K) CARS images, (B,G,L) SHG/TPF images, (C,H,M) an integrated Raman intensity of cells in the 2850−3050 cm^{-1} region and (D,I,N) in the 785−805 cm^{-1} region, and (E,J,O) Papanicolaou-stained images. Reproduced from Aljakouch, K.; Hilal, Z.; Daho, I.; Schuler, M.; Krauß, S. D.; Yosef, H. K.; Dierks, J.; Mosig, A.; Gerwert, K.; El-Mashtoly, S. F. *Anal. Chem.* **2019**, *91*, 13900−13906 (ref 132). Copyright 2019 American Chemical Society. (P) Comparison of the Raman difference spectrum (normal−cancer) of urothelial cells (b) with the Raman spectra of pure compounds of glycogen (a) and oleic acid (c). Reproduced from Yosef, H. K.; Krauß, S. D.; Lechtonen, T.; Jütte, H.; Tannapfel, A.; Käfferlein, H .U.; Brüning, T.; Roghmann, F.; Noldus, J.; Mosig, A.; El-Mashtoly, S. F.; Gerwert, K. *Anal. Chem.* **2017**, *89*, 6893−6899 (ref 135). Copyright 2017 American Chemical Society.

increased the demand for cost-effective and fast alternative tools to the currently used method in clinical practice.

Raman spectroscopy has been employed in several cellular applications, including the identification of different cell types. It has significant potential for clinical translation as an adjunctive method for the diagnosis of precancerous and cancerous lesions. Although there are few Raman studies on Pap smears, spontaneous Raman spectroscopy has shown the potential for cervical cancer recognition using the biochemical fingerprint of cells.[128] For instance, it has been reported that few Raman spectra from the cellular nuclei can distinguish between normal and abnormal Pap-smears using PCA-LDA and PLS-DA with high accuracy.[129] In addition, spontaneous Raman spectroscopy discriminates between transient (n = 30) and persistent HPV infection (n = 30). PLS-DA classification model based on the mean spectra of the sample provided a sensitivity and specificity of 90% and 100%, respectively, for the classification of transient and persistent HPV infection.[130]

Furthermore, a recent study employed SERS using gold nanoparticles as a substrate to differentiate between normal (n = 47), high-grade squamous intraepithelial (HSIL, n = 41), and cervical squamous cell carcinoma (CSCC, n = 36) Pap smears.[131] The authors performed SERS measurements in the fingerprint region using three strategies: single cells, cell pellet, and extracted DNA. The results revealed molecular changes in carotenoids, amino acids, and nucleic acids during cervical cancer progression. The classification model based on SVM produced an accuracy of approximately 94%, 71%, and 97% using single cells, cell pellets, and DNA, respectively.[131] These results indicate that single cells or DNA measurements provide the highest accuracy.

All the above approaches were dependent on monitoring changes in the cellular composition. Aljakouch et al. recently used Raman spectral imaging and DCNNs to discriminate between normal (n = 10), low-grade squamous intraepithelial (LSIL, n = 10), and high-grade squamous intraepithelial (HSIL, n = 10) with 100% accuracy.[132] This approach is based not only on the integral biochemical composition of the whole cell but also on the cellular morphological features obtained from Raman spectral images at six wavenumbers, enabling classification with higher accuracy. Aljakouch et al. reported a

new approach in which CARS, SHG/TPEF, and DCNNs were applied to identify cancerous cervical cells in Pap smears.[132] In these images (Figure 5A), the cell nuclei were visible and the nucleus to cytoplasm ratio could be calculated to distinguish between normal, LSIL, and HSIL cells as used in the Pap test.[133,134] The discrimination between normal and cancerous cells was achieved automatically with 100% accuracy based on the morphological features obtained from CARS/SHG/TPEF images at one wavenumber (2935 cm^{-1}). Thus, high accuracy can be achieved for differentiation between various Pap smears by applying fast CARS/SHG/TPEF imaging at a single wavenumber instead of using Raman spectral imaging. Therefore, nonlinear microscopic imaging has great potential for evaluating large cell numbers in Pap smears. However, it is still necessary to apply either the SERS or CARS/SHG/TPEF imaging approaches in a multicenter workflow to verify the conclusions of this approach before considering its application in clinical practice; the above approach is applied in a similar way for the diagnosis of bladder cancer using urine sediments.[135] Since bladder cancer is often to recur, patients with a history of, for example, NMIBC are regularly subject to follow-up to control recurrence after therapies.[136,137] Cystoscopy and urine cytology still form the backbone of diagnosis and follow-up for bladder cancer. Cystoscopy is an invasive diagnostic procedure that is perceived as uncomfortable in almost all patients. This may ultimately lead to patients avoiding follow-up. In addition, urine cytology is highly dependent on the expertise of the examiner and has limited sensitivity, especially for well-differentiated tumors.[138] For high-grade NMIBC, the specificity and sensitivity of cytology are ≥90% and ∼80%, respectively, while in the case of low-grade NMIBC, the sensitivity is low (∼20−53%).[139,140] Consequently, there is an urgent request to establish a noninvasive tool for bladder cancer diagnosis and screening for bladder cancer recurrence. Yosef et al. developed a noninvasive approach based on this purpose, and it includes spontaneous Raman imaging of urothelial cells in urine sediments collected from patients diagnosed with high-grade urothelial carcinoma (n = 10) and from patients with pathologically confirmed urocystitis (n = 10).[135,141] Random forest classifier and DCNNs methods were used to distinguish
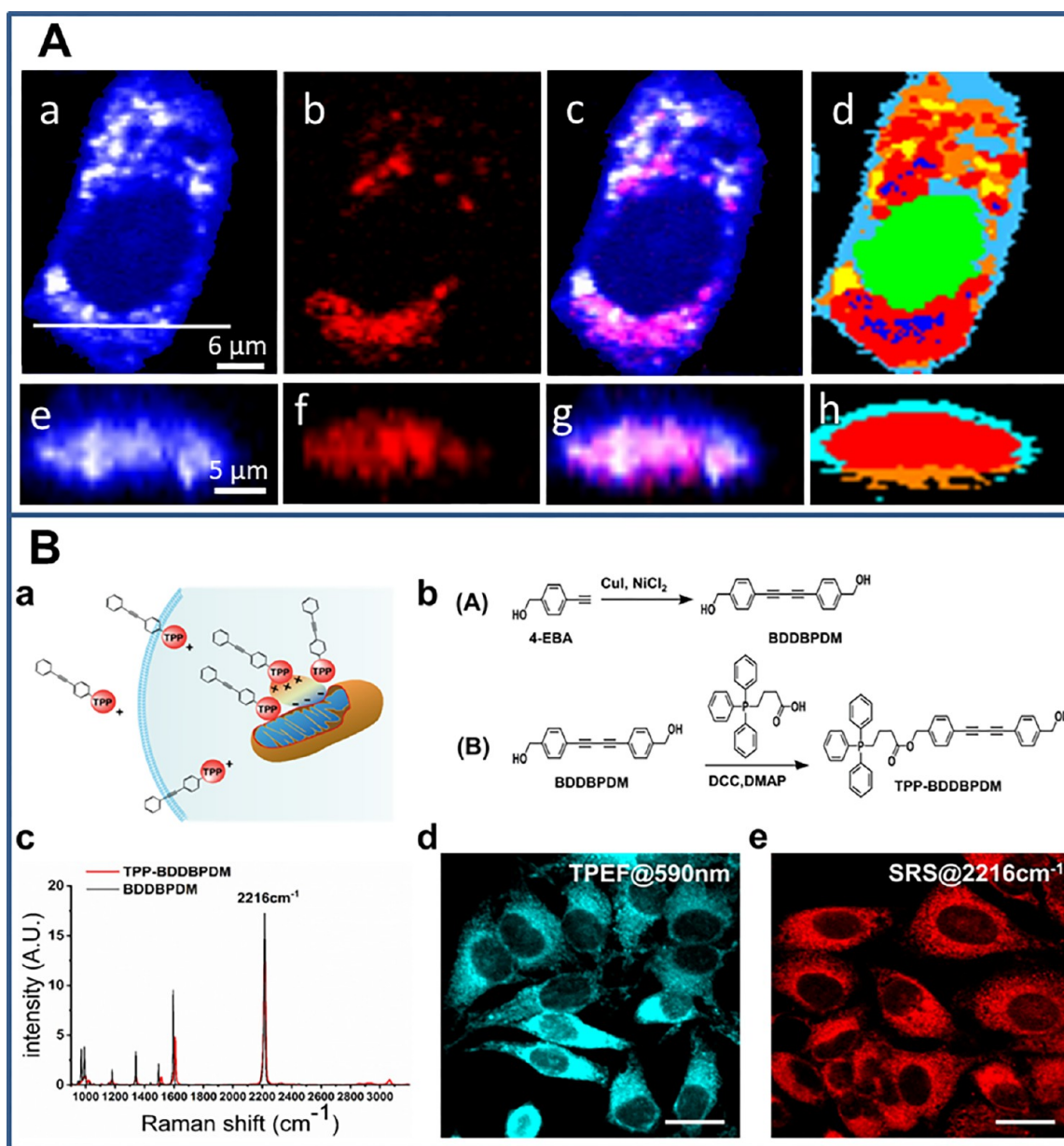
Figure 6. (A) Raman imaging of SK-BR-3 cells treated with neratinib. Raman images reconstructed from the C−H deformation (a) and C≡N stretching (b) intensities. (c) Overlay of panels a and b. (e−g) Cross-sectional Raman images of the same cell measured along the $x-z$ axis. Scanning positions are indicated by the white line in panel a. (d,h) HCA results based on Raman data shown in panels a and e. Reproduced from Raman Microspectroscopic Evidence for the Metabolism of a Tyrosine Kinase Inhibitor, Neratinib, in Cancer Cells, Aljakouch, K.; Lechtonen, T.; Yosef, H. K.; Hammoud, M. K.; Alsaidi, W.; Kötting, C.; Mggge, C.; Kourist, R.; Samir F. El-Mashtoly, S. F.; Gerwert, K. *Angew. Chem. Int. Ed. Engl.*, Vol. 57, Issue 24, 7250−7254 (ref 148). Copyright 2018 Wiley. (B) Characterization of TPP-BDDBPDM. (a) Schematic of the binding mechanism of TPP to mitochondria. (b) Synthesis steps for BDDBPDM and TPP-BDDBPDM. (c) Spontaneous Raman spectra of BDDBPDM (black) and TPP-BDDBPDM (red) in the silent region with a step size of 0.8 cm^{-1}. HeLa cells are stained with JC-1 (2 μM) and TPP-BDDBPDM (50 μM) in culture medium for (d) fluorescence and (e) SRS images at 2216 cm^{-1}. Scale bars = 10 μm. Reproduced from Bae, K.; Zheng, W.; Ma, Y.; Huang, Z. *Anal. Chem.* **2020**, *92*, 740−748 (ref 153). Copyright 2020 American Chemical Society.

between cancerous and noncancerous urothelial cells, and the results showed that the accuracy of the classifications based on DCNNs exceeds other classifiers.[135,142]

The reason for such high accuracy is that the DCNN classifications were relying not only on the spectral information but also on the morphological features of the cells. Furthermore, the Raman results showed that the glycogen band, 482 cm^{-1}, can be used to distinguish normal and high-grade cancerous urothelial cells, as shown in Figure 5B. This is because the glycogen level in normal urothelial cells is higher

than that in cancer cells. The Raman results also suggest that the levels of fatty and nucleic acids increase in cancer cells. Thus, the Raman results indicate metabolic changes in cancer cells at a molecular level.[135] These preliminary results were part of the Uro*Follow* trial, which is a prospective randomized study comparing noninvasive follow-up of patients with pTa G1-2/low-grade NMIBC using commercially available urine markers along with abdominal ultrasound vs cystoscopy.[143]

■ RAMAN SPECTROSCOPY FOR THERAPY

Drug Pharmacokinetics in Single Cells. Remarkable efforts have been made to improve the development of anticancer drugs.[144] However, the attrition rates of anticancer drugs are high during development, which is an obstacle in the pharmaceutical industry.[145] Since drug development is a costly, time-consuming, and high-risk endeavor, innovative approaches are necessary to obtain new drug candidates and decrease the current high attrition rates. Imaging modalities analyze and quantify the influence of drugs on biological processes at the molecular and cellular levels in living systems. Therefore, it can play a crucial role in various phases of drug development, including screening of drug candidates and accelerating the preclinical medicinal chemistry optimization cycles as well as improving the *in vitro* to *in vivo* translation of drug candidates.[146] For instance, fluorescence imaging visualizes fluorescently labeled molecules, including proteins, nucleic acids, antibodies, and small-molecule drugs. However, fluorescent labels are usually larger than small-molecule drugs and can considerably change the pharmaceutical activity of the drug. In contrast, label-free vibrational microscopic tools can visualize drug candidates based on the intrinsic molecular contrast. Raman imaging offers new possibilities for monitoring the uptake, distribution, and metabolism of drug candidates in cells or tissues with subcellular spatial resolution.

Label-free imaging of the uptake of drugs is very challenging utilizing spontaneous Raman microscopy because drugs regularly accumulate inside cells at lower concentrations. To enhance the Raman selectivity, several research groups have used functional groups, such as alkynes, nitriles, carbonyls, and isotopic labels (deuterium) in the drug molecules as label-free markers since these groups have Raman bands in the silent region of the cell spectrum (1800−2800 cm^{-1}). For example, El-Mashtoly et al. applied spontaneous Raman spectral imaging to visualize the spatial distribution of tyrosine kinase inhibitor (TKI) erlotinib, containing an inherent alkyne group in its chemical structure, within the cell.[147] The Raman results suggest that erlotinib is metabolized to desmethyl erlotinib metabolite.[147] Furthermore, Aljakouch et al. reported the spatial distribution and metabolism of TKI, neratinib containing an inherent nitrile group, in various cancer cells using spontaneous Raman spectral imaging (Figure 6A).[148] Fluorescence imaging indicated that neratinib accumulated in lysosomes as well as the internalization of the drug targets, EGFR, and HER2 receptors. This study used Raman, density functional theory (DFT) calculations, and fluorescence microscopy to monitor the drug distribution and metabolism and to visualize drug localization as well as the drug targets in cells.

Raman intensity can be enhanced for small-molecule drugs in cells using coherent Raman microscopy, since SRS has greater sensitivity and can be employed at a video rate. Sepp et al. monitored the uptake and distribution of TKI ponatinib, containing alkyne group, in cell models of ponatinib resistance.[149] The detection of ponatinib, approved for the treatment of chronic myeloid leukemia, achieved at nanomolar concentrations, allows the determination of differences in uptake and sequestration into lysosomes during the development of acquired drug resistance.[149,150] Furthermore, SRS imaging of Raman tags is applied as a general approach for examining a wide spectrum of small molecules in cells and animals.[151] For instance, Min et al. employed a conjugated diyne with a terminal phenyl ring as a Raman tag (2251 cm^{-1}) to investigate the distribution of the anticancer antimycin-type depsipeptides, a complex natural product, in single live cells.[152] Taken together, these efforts shed light on the great potential of Raman-tag imaging in anticancer drug pharmacokinetics research. Recently, Bae et al. used a Raman tag based on conjugated diyne with terminal phenyl rings (2216 cm^{-1}) to monitor in real-time and quantify triphenylphosphonium (TPP), a mitochondria-targeting agent, to trace mitochondrial dynamics in live cells (Figure 6B).[153] These results demonstrate the prospective for real-time screening of pharmacokinetics and improving the growth of mitochondria-targeting imaging probes and treatments in the future.

Small-molecule inhibitors exhibit strong and sharp Raman bands in the fingerprint region, which can be applied as a label-free marker to detect their distribution in cells.[154] For instance, Aljakouch et al. utilized a Raman peak in the fingerprint region, 1386 cm^{-1}, to monitor neratinib in different cancer cells.[148] Rammal et al. observed the distribution of doxorubicin (DOX) and its squalenoylated nanoparticles in cancer cells using Raman marker bands, 1211 and 1241 cm^{-1}, in the fingerprint region.[155] In addition, Fu et al. described SRS imaging and quantification of TKIs imatinib and nilotinib using Raman peaks ∼1300 cm^{-1}; in addition, the process of drug uptake into lysosomes was monitored simultaneously using TPEF.[156] Dong et al. also employed polarization-sensitive SRS from C≡C stretching vibration in the fingerprint region of amphotericin B (AmB), an antifungal agent, to monitor its distribution in fungal cells.[157] The results showed that AmB is located in the cell membrane and highly ordered, and its orientation is primarily parallel to phospholipid acyl chains, supporting that AmB vertically forms a transmembrane tunnel, the classical ion channel model.[157] These results propose a platform for promoting low-toxicity and resistance-refractory antifungal agents. Coherent Raman scattering microscopy provides a mapping approach of drug molecules inside a cell but with sensitivity limited to millimolar concentrations for endogenous molecules by employing near-infrared (NIR) pulse excitation.[149,156] Zhuge et al. applied visible preresonance SRS microscopy and significantly boosted the molecular sensitivity for visualizing retinoids to 34 μM based on vibrational fingerprint signatures. This was achieved by choosing the wavelength of excitation in the visible region near the electronic transitions of the intrinsic chromophores. This report revealed a heterogeneous distribution of retinoids within cancer cells.[158]

Raman Imaging of Intracellular Nanocarriers. Nanocarriers are employed as drug delivery vehicles to improve drug bioavailability and biocompatibility and to target diseased tissues. Nanocarriers allow the administered drug dosage to be reduced, leading to safer therapy. They can also enter the cell, deliver their load, and be internalized by cells. Accordingly, it is important to monitor their internalization and cellular distribution to infer their function as drug carriers.[159] Raman microscopy has been applied to label-free imaging of nanocarriers. Vanden-Hehir et al. synthesized alkyne-tagged and deuterated poly(lactic acid-*co*-glycolic acid) and monitored their distribution in primary rat microglia using SRS microscopy.[160] In addition, the alkyne nanoparticles were imaged in the tissue of *ex vivo* cortical mouse brain tissue.[160] Bugárová et al. demonstrated that the bioconjugation of graphene oxide (GO) nanocarriers to biotinylated M75 antibody is very specific to the transmembrane protein

N
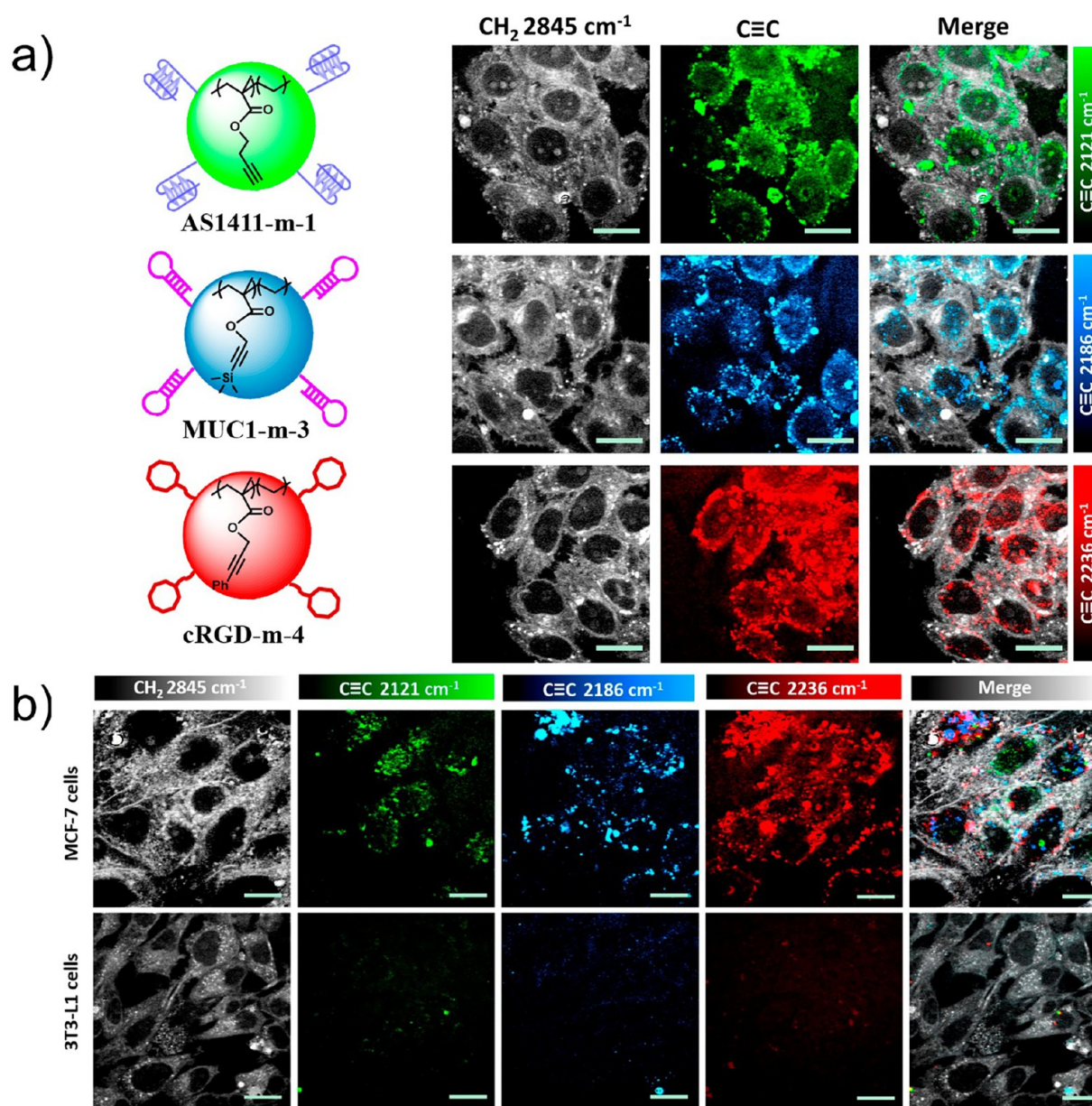
Figure 7. (a) Three-color targeted Raman beads, m-1 (2121 cm^{-1}), m-3 (2186 cm^{-1}), and m-4 (2236 cm^{-1}), were incubated separately with MCF-7 cells. The images at 2845 cm^{-1} are lipid CH$_2$ channels showing cell morphology. (b) AS1411-m-1 (2121 cm^{-1}), MUC1-m-3 (2186 cm^{-1}), and cRGD-m-4 (2236 cm^{-1}) were incubated simultaneously with MCF-7 and 3T3-L1 cells. Scale bars: 20 μm. Reproduced from Jin, Q. Q.; Fan, X.; Chen, C.; Huang, L.; Wang, J.; Tang, X. *Anal. Chem.* **2019**, *91*, 3784−3789 (ref 162). Copyright 2019 American Chemical Society.

carbonic anhydrase, which is expressed by tumor cells.[161] In addition, 3D Raman imaging at the cellular level was utilized to track GO nanocarrier endocytosis.

Jin et al. synthesized polymeric nanoparticles with monomers including alkyne, cyanide, azide, and carbon-deuterate that produce Raman peaks in the cell-silent region (1800−2800 cm^{-1}) for molecular targeting (Figure 7).[162] A library of Raman beads for wavenumber multiplexing was also built, demonstrating five-color SRS imaging of mixed nanoparticles with different Raman wavenumbers. Furthermore, Raman beads anchored with targeting moieties, including nucleic acids, aptamers, and peptides, were applied to tumor targeting in cancer cells and tissues. Spontaneous Raman imaging was employed to monitor tumors in live mice without the need for any intensity improvement because of the high density of Raman reporters in Raman beads.[162]

Drug Pharmacokinetics in Skin. There is still unmet therapeutic demand for the treatment of skin diseases due to poor drug delivery. The approach of topical drug delivery may be efficient to treat skin diseases since the active formulation can be locally utilized in the injured region. Therefore, human skin is considered a vital road for drug delivery. Noninvasive imaging modalities, such as Raman methods, offer advances to regular tape stripping,[163] which is applied to explore the penetration of the small-molecule drugs into the skin.[164] For instance, Santos et al. monitored the penetration of two vitamin derivatives: retinyl acetate and alpha-tocopheryl acetate into the stratum corneum of young (24.1 ± 3.3 years old) and elderly (68 ± 5.8 years old) participants using spontaneous Raman spectroscopy.[165] The results indicated that the vitamins penetrated the stratum corneum (24 μm) in both study groups. However, the penetration was mostly
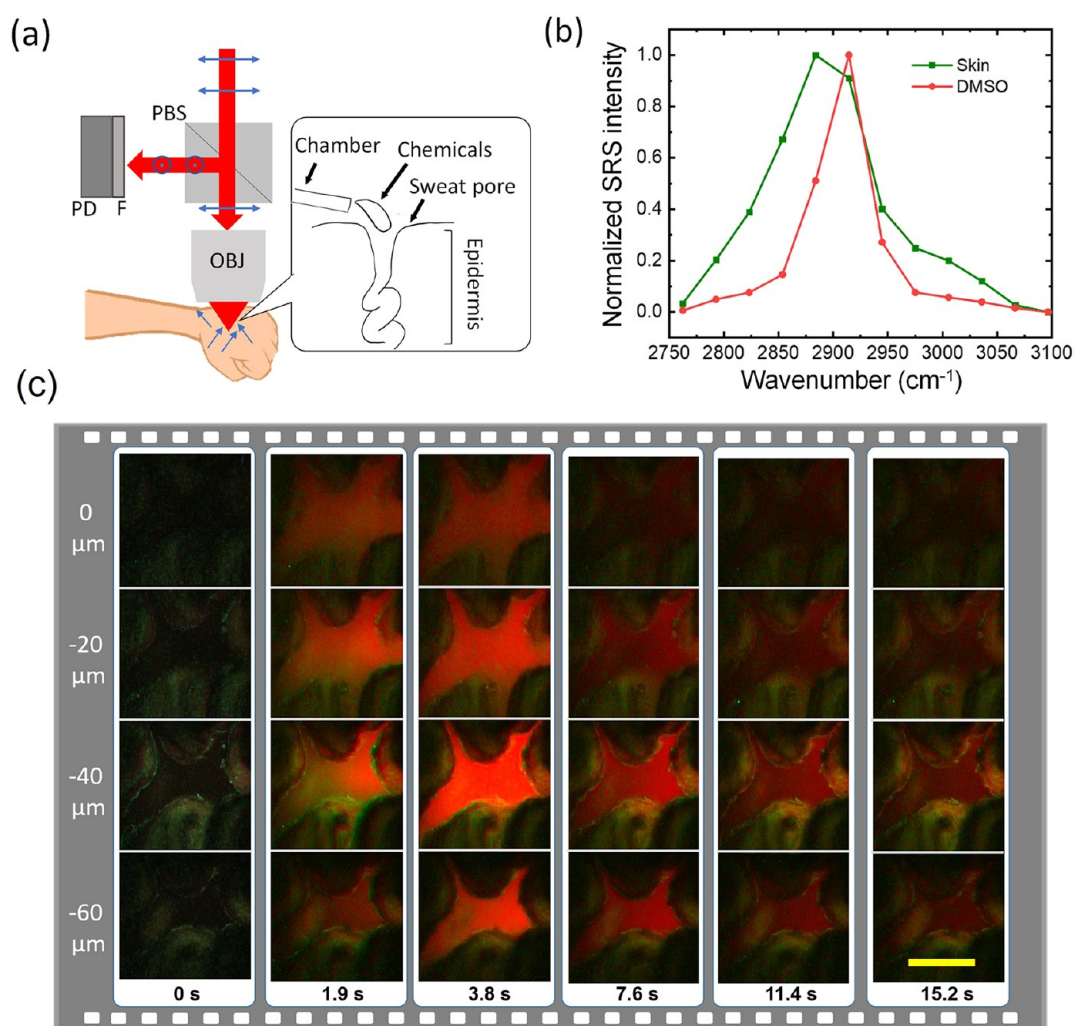
Figure 8. Recording chemical penetration into a human sweat pore. (a) An add-on setup for epi-detected SRS imaging *in vivo*, including a polarization beam splitter (PBS), a photodiode (PD), and short-pass-filter (F). The blue arrows represent the polarization of the beams. The inner box is a schematic of DMSO dropped into a human sweat pore through a plastic chamber. (b) SRS spectra of human skin and DMSO. (c) Two-color volumetric imaging of DMSO penetrating a sweat pore. Green and red represent skin at 2884 cm^{-1} and DMSO at 2914 cm^{-1}, respectively. Scale bar: 100 μm. Reprinted with permission from ref 172. Copyright The Optical Society. *Optics Express* 28, 30210 (**2020**).

affected by the stratum corneum composition.[165] In addition, Caspers et al. developed a method based on confocal Raman spectroscopy to determine the concentration of *in vivo* skin penetration of applied compounds such as trans-retinol and propylene glycol as well as the flux of these compounds through the stratum corneum.[166]

Furthermore, SRS microscopy was applied almost a decade ago to monitor and depict the uptake of drugs into mice and human skin in real-time.[20,167] The Schäfer-Korting group examined the penetration of dexamethasone from an ethanolic hydroxyethyl cellulose gel into *ex vivo* human skin, murine skin, and reconstituted human skin using several techniques, including SRS.[168] SRS determined the ethanol-induced differences in the ratio of protein-to-lipid in the stratum corneum and accurately dissected the penetration-enhancing effects of ethanol.[168] Feizpour et al. used a combination of SRS imaging and deep learning to determine the flow and flux of drugs within the layers and structures of the skin of the nude mouse ear.[169,170] Pharmacokinetic parameters through CNN of SRS images were extracted, revealing a new avenue for pharmacokinetics of, for example, skin cancer.[169,170] Interestingly, Sarri et al. performed CARS and TPEF imaging to

determine the percutaneous penetration of glycerol diluted in water and xanthan gel into human skin *in vivo*. The results suggest that xanthan gel maintains glycerol on the skin surface, allowing its constant release.[171] In addition, Lin et al. constructed a deformable mirror-based remote-focusing SRS system, enabling excellent volumetric imaging of the skin (Figure 8).[172] In this study, the authors obtained the dynamic diffusion of drugs in real-time into human sweat pores, which were suggested to disrupt the *stratum corneum* barrier and deliver the drugs into the epidermal layer.[172]

Cell-Based Therapy. Cell-based therapy is considered a strategy for the treatment of many human diseases. There have been major advances in this field, which have been applied to several diseases over the last 2 decades. Generally, it includes the injection or living cells implantation into a patient to accomplish a curative objective. In order to manufacture a product based on cell therapy, it is necessary to understand the basics of cellular biochemical and functional characteristics, and the therapeutic product must be safe and efficient. Raman spectroscopy is very suitable as a quality control tool for cell-based therapy due to the following: (i) it is a label-free and nondestructive method, allowing the measurements and
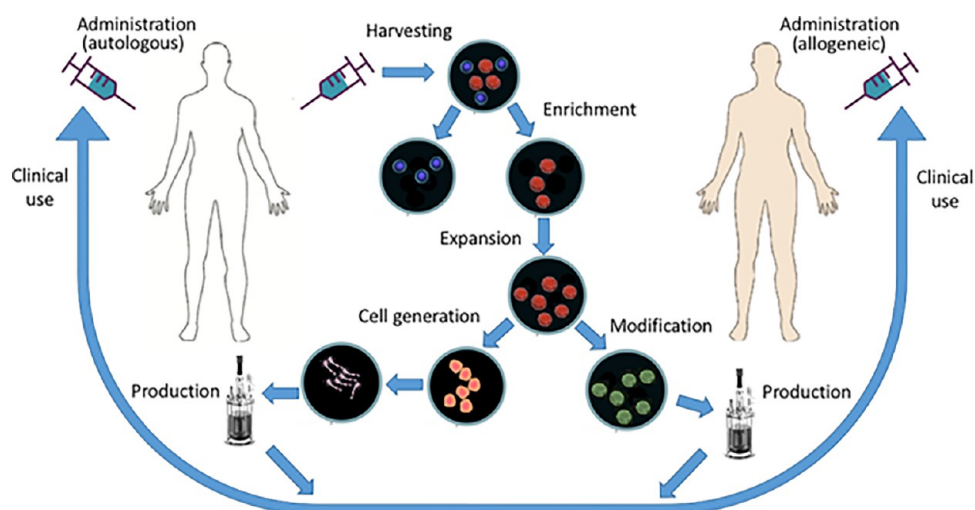
Figure 9. Schematic illustration of cell therapy bioprocessing and research. Manufacturing processes generally require substantially scaled-up versions of each stage once these have been selected through basic research. Clinical adoption should only follow rigorous safety and efficacy evaluations through randomized clinical trials using the manufactured cells. Reproduced from Rangan, S.; Schulze, H. G.; Vardaki, M. Z.; Blades, M. W.; Piret, J. M.; Turner, R. F. B. *Analyst* **2020**, *145*, 2070−2105 (ref 173), with permission of The Royal Society of Chemistry.
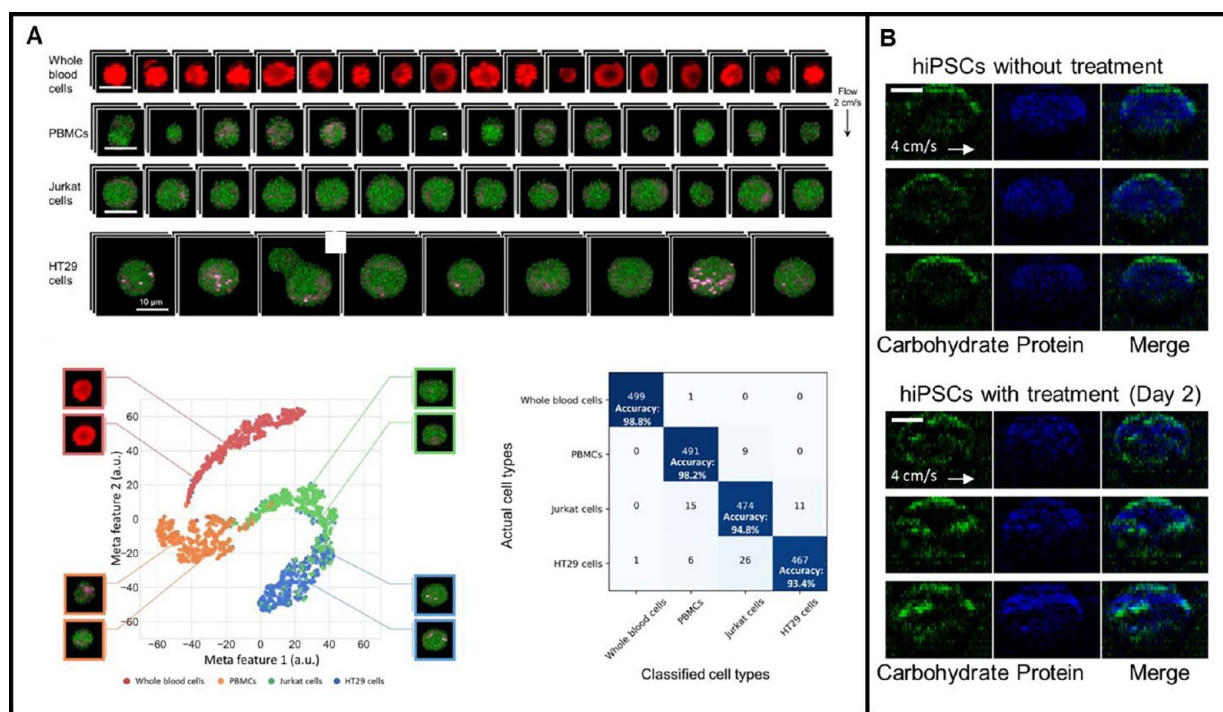
Figure 10. (A) SRS imaging flow cytometry and label-free cancer cell detection in liquid biopsy. (a) SRS images of whole blood cells, PBMCs, Jurkat cells, and HT29 cells. Green, protein; pink, lipids; red, hemoglobin. (b) t-SNE plot of the cells after the CNN is applied to the acquired SRS images of the cells. Insets show typical SRS images of each cell type. (c) Confusion matrix of the cells. (d) SRS images of cells classified by the CNN as HT29 cells and PBMCs with prediction probabilities in the sample of HT29 cells spiked in PBMCs. Reproduced with permission from *Proceedings of the National Academy of Sciences USA* Suzuki, Y. et al., *Proc. Natl. Acad. Sci. U.S.A.* **2019**, *116*, 15842−15848 (ref 181). (B) SRS images of hiPSCs cultivated in two different culture media for the naïve pluripotent state (with 2 days of treatment, *n* = 1699) and the primed pluripotent state (without treatment, *n* = 1641). Reprinted by permission from Macmillan Publishers Ltd.: NATURE Communications, Nitta, N. et al., *Nature Communications* **2020**, *11*, 3452 (ref 182). Copyright 2020.

characterization of living cells, and (ii) water exerts minimal interference on the Raman spectrum; thus, it can be used for measuring cells in media or buffers.[173]

The cell-based therapy strategy mainly includes the following fields: (i) basic research, (ii) production processes and product formulation, and (iii) clinical research and clinical applications.[173] The basic research field focuses on cell

harvesting, expansion, and generation as well as cell characterization (Figure 9). According to the literature, Raman spectroscopy is primarily utilized for the cell characterization stage in the application of cell-based therapy. For instance, Baradez et al. used spontaneous Raman spectroscopy and chemometric models to monitor changes during bioprocessing of T-cells and the concentrations of biomolecules, such as

glucose, glutamate, and lactate. Further, cell concentration and viability markers can be tracked in real-time.[174] These findings show the prospective of Raman methods as a new process analytical technology for monitoring, for example, the consumption of nutrients and the production of metabolites.

Therapies based on stem cells have recently emerged for the treatment of several incurable diseases. Before therapy, different types of derived stem cells and their functions should be investigated in detail. Suhito et al. used a combination of autofluorescence and label-free spontaneous Raman mapping to characterize mesenchymal stem cells (MSCs) as a model and caused adipogenesis.[175] On the one hand, autofluorescence revealed information regarding morphology and cytosolic microstructures of cells. On the other hand, Raman imaging permits site-specific analysis of target molecules, allowing large-scale screening of differentiation variability.[175] In another study, Hsu et al. demonstrated that human induced pluripotent stem cells (hiPSCs) can be distinguished from iPSC-derived neural cells using a Raman biomarker of glycogen.[176] Using a classification model built on Raman data, hiPSCs in different developmental stages were classified with 97.5% accuracy. Interestingly, this model can be applied to other cell types. Such a Raman-based classification model could have a high impact on cell sorting and quality control of cell-based therapy.[176]

Furthermore, Hua et al. developed a hybrid nanostructured substrate for combined SERS and near-infrared fluorescence imaging to observe with high precision the MSCs behavior.[177] The fluorescence imaging and SERS revealed the distribution and metabolism of the transplanted MSCs. SERS imaging delineated the MSCs from the boundaries of normal tissues with high precision, even at single-cell resolution. This methodology shows the potential for monitoring stem cells in various regenerative medicine applications.[177]

It is worth mentioning that flow cytometry is a robust method with utilization in various areas, and it may also contain cell sorting capability to subsequently analyze the sorted sample. However, it primarily depends on fluorescent labeling for cellular phenotyping, which needs time-consuming preparation protocols.[178−182] Therefore, it is not suitable for cell-based therapy. For instance, the fluorescently labeled hiPSCs and CAR-T cells cannot be injected into humans for therapy.[178−182] Coherent Raman microscopy is suitable for evaluating cells employed in cell therapy because it can perform label-free assessments of cells with high throughput. Several research groups recently developed Raman flow cytometry-based analysis of label-free coherent Raman microscopy (Figure 10A) as well as Raman image-activated cell sorting (RIACS).[178−182]

Nitta et al. acquired SRS imaging of naïve and primed hiPSC underflow, displaying variations in the distribution of carbohydrates and proteins (Figure 10B).[182] SRS imaging confirmed an increase in the carbohydrate level in primed hiPSCs, which can be considered a biomarker for the primed state.[182] RIACS has several possible applications, including quality control of cells for cell therapies, such as hematopoietic stem cell transplantation, mesenchymal stem cell therapy, CAR-T therapy, and hiPSC therapy.[182]

■ CONCLUSIONS

Raman spectroscopic methods offer new prospects for disease diagnostics and drug discovery. The current review highlights the significant studies that have been conducted since 2019,

employing different Raman spectroscopic tools. The applications include diagnosis and screening of several diseases using different samples, such as urine, blood, tears, smears, cells, and tissue biopsies. This can be achieved by identifying, for example, cancer cells and recognition of pathological tissues. In addition, these applications shed light on drug metabolism in cells and skin. The Raman fingerprint of the cell, tissue, or liquid biopsy is an excellent metabolic indicator that reveals the molecular basis of the disease, enabling quantification of the molecular information for diagnosis and therapy evaluation. However, there is still a need for improvement before bringing the method into clinical settings and drug discovery.

For developing a diagnostic tool, it is necessary to standardize the Raman spectroscopic platforms for all operators. This includes experimental conditions, such as spectrometer calibration, which instrument to employ, excitation wavelength, laser power, as well as unifying the parameters used in data analysis. To address this issue, a recent study presented a round-robin experiment examining the comparability of several Raman instruments with various configurations from five different manufacturers in a multi-center study (Raman4clinics).[183] Such large collaboration or even broader is essential to decrease the differences in the devices used in different institutions and standardize the Raman setup.

Furthermore, spontaneous Raman scattering is described by low sensitivity due to its weak intensity. As a result, the physiological concentration of, for example, the disease biomarker or drug in many cases is lower than the detection limit. This also leads to employing a small sample pool in some of the studies reported in this review. The utilization of CRS in addition to new hyperspectral and multiplex CRS microscopy is anticipated to improve the detection limit and offer high-speed imaging, enabling larger sample numbers to be investigated, as well as the integration of multimodal nonlinear optical microscopic tools such as TPEF and SHG. Therefore, CRS can be used to validate several Raman applications in diagnostics using a large cohort in a multi-institution approach to further confirm the previous results. In addition, approaches based on deep learning are evolving rapidly and represent promising tools to improve our current way of diagnosing and treating diseases in terms of speed, objectivity, as well as reproducibility.[3] Thus, the combination of CRS and nearly real-time deep learning approaches have great potential for medical diagnostics in the near future.

Moreover, several small-molecule drugs with a Raman tag in the cell-silent region have been investigated using Raman and SRS imaging. Only a few studies have reported the distribution of drug candidates in cells using label-free marker bands in the fingerprint region. The advantage of this approach is that a large number of drug candidates without Raman tags in the cell silent region can be screened in a label-free manner. However, the detection of these drug candidates could be very challenging in living cells at physiological concentrations. Therefore, it is necessary to monitor the distribution and metabolism of several drug candidates that do not have a Raman tag in the cell silent region by rapid SRS imaging to confirm the capability of SRS to detect such compounds. Finally, assessing drug candidates' distribution and metabolism can be thoroughly investigated using nonlinear microscopy, including both SRS imaging and TPEF with fluorescence labeling of cellular components or proteins. This will determine the drug accumulation in certain cellular compo-

nents as well as monitoring the drug targets. This provides significant information on the drug mechanism of action and target engagement.[149,150] With the above-mentioned combinations, patients will profit from rapid and precise diagnoses and therapy response monitoring. Further, these options will propose novel therapeutics to patients.

■ AUTHOR INFORMATION

Corresponding Author

Samir F. El-Mashtoly − *Center for Protein Diagnostics and Department of Biophysics, Faculty of Biology and Biotechnology, Ruhr University Bochum, 44801 Bochum, Germany;* ⊙ orcid.org/0000-0001-6087-8817; Email: samir.el-mashtoly@rub.de

Author

Klaus Gerwert − *Center for Protein Diagnostics and Department of Biophysics, Faculty of Biology and Biotechnology, Ruhr University Bochum, 44801 Bochum, Germany;* ⊙ orcid.org/0000-0001-8759-5964

Complete contact information is available at:
https://pubs.acs.org/10.1021/acs.analchem.1c04483

Notes

The authors declare no competing financial interest.

Biographies

Samir F. El-Mashtoly is leading the Raman imaging group at the Department of Biophysics, PRODI, Ruhr University, Bochum, Germany. He received his B.Sc. and M.Sc. in Chemistry from Ain Shams University, Egypt. He also obtained his Ph.D. in Chemistry from Tohoku University, Japan. He was a JSPS Fellow at the Okazaki Institute for Integrative Bioscience, Japan, and a Research Associate at the Albert Einstein College of Medicine, U.S. Additionally, El-Mashtoly was appointed as an Assistant Professor at King Khalid University, Saudi Arabia, and Zewail City of Science and Technology, Egypt. His research focuses on understanding the structure−function relationship in sensor proteins. In addition, he is developing tools for the assessment of cancer therapy and noninvasive diagnostic methods for cancer using Raman spectroscopy. Finally, he is interested in biomarker research in neurodegenerative diseases.

Klaus Gerwert studied Physics and graduated in Biophysical Chemistry. After positions at Max-Planck and the Scripps Research Institutes, U.S., and honored by a Heisenberg-fellowship of the German Science Foundation (DFG), he accepted a university professorship and Chair in Biophysics at Ruhr-University Bochum (RUB). He was a Fellow of the Max Planck Society and has been an external director at the Max Planck Partner Institute in Shanghai. Currently, he is the founding director of PRODI, a federal/state-financed research center for protein diagnostics at RUB. Gerwert actively promotes the development and application of Raman and infrared spectroscopy in protein research in over 200 publications with over 10 000 citations and several patents. He is internationally recognized for his studies on detailed protein reaction mechanisms, especially the functional role of protein-bound water molecules. He recently focused on the application of quantum cascade laser-based IR imaging of cancer and brain tissue. His current interest is the translation of his invented immuno-IR-sensor into the clinic, which uses protein misfolding as a biomarker to identify early stage neurodegenerative diseases in liquid biopsies, especially symptom-free Alzheimer's, in a blood test.

■ ACKNOWLEDGMENTS

■ REFERENCES

(1) Pradhan, P.; Guo, S.; Ryabchykov, O.; Popp, J.; Bocklitz, T. W. *J. Biophotonics* **2020**, *13* (6), e201960186 DOI: 10.1002/jbio.201960186.

(2) Zantalis, F.; Koulouras, G.; Karabetsos, S.; Kandris, D. *Future Internet* **2019**, *11* (4), 94.

(3) He, H.; Yan, S.; Lyu, D.; Xu, M.; Ye, R.; Zheng, P.; Lu, X.; Wang, L.; Ren, B. *Anal. Chem.* **2021**, *93* (8), 3653−3665.

(4) Binkhonain, M.; Zhao, L. *Expert Systems with Applications: X* **2019**, *1*, 100001.

(5) Krafft, C.; Schmitt, M.; Schie, I. W.; Cialla-May, D.; Matthäus, C.; Bocklitz, T.; Popp, J. *Angew. Chem., Int. Ed.* **2017**, *56* (16), 4392−4430.

(6) Tipping, W. J.; Lee, M.; Serrels, A.; Brunton, V. G.; Hulme, A. N. *Chem. Soc. Rev.* **2016**, *45* (8), 2075−2089.

(7) Kong, K.; Kendall, C.; Stone, N.; Notingher, I. *Adv. Drug Delivery Rev.* **2015**, *89*, 121−134.

(8) Baker, M. J.; Hussain, S. R.; Lovergne, L.; Untereiner, V.; Hughes, C.; Lukaszewski, R. A.; Thiéfin, G.; Sockalingum, G. D. *Chem. Soc. Rev.* **2016**, *45* (7), 1803−1818.

(9) Baker, M. J.; Byrne, H. J.; Chalmers, J.; Gardner, P.; Goodacre, R.; Henderson, A.; Kazarian, S. G.; Martin, F. L.; Moger, J.; Stone, N.; Sulé-Suso, J. *Analyst* **2018**, *143* (8), 1735−1757.

(10) Raman, C. V.; Krishnan, K. S. *Nature* **1928**, *121* (3048), 501−502.

(11) Ember, K. J. I.; Hoeve, M. A.; McAughtrie, S. L.; Bergholt, M. S.; Dwyer, B. J.; Stevens, M. M.; Faulds, K.; Forbes, S. J.; Campbell, C. J. *npj Regen Med.* **2017**, *2* (1), 12.

(12) Diem, M. G. *Vibrational Spectroscopy for Medical Diagnosis*; Diem, M. G., Ed.; Wiley & Sons, 2008.

(13) Popp, J. *Handbook of Biophotonics*, Vol. 2: Photonics for Health Care; Wiley-VCH: Weinheim, Germany, 2011.

(14) Okada, M.; Smith, N. I.; Palonpon, A. F.; Endo, H.; Kawata, S.; Sodeoka, M.; Fujita, K. *Proc. Natl. Acad. Sci. U. S. A.* **2012**, *109* (1), 28−32.

(15) Matousek, P.; Towrie, M.; Ma, C.; Kwok, W. M.; Phillips, D.; Toner, W. T.; Parker, A. W. *J. Raman Spectrosc.* **2001**, *32* (12), 983−988.

(16) Cialla-May, D.; Zheng, X.-S.; Weber, K.; Popp, J. *Chem. Soc. Rev.* **2017**, *46* (13), 3945−3961.

(17) Fan, M.; Andrade, G. F. S.; Brolo, A. G. *Anal. Chim. Acta* **2020**, *1097*, 1−29.

(18) Jeanmaire, D. L.; Van Duyne, R. P. *J. Electroanal. Chem. Interfacial Electrochem.* **1977**, *84* (1), 1−20.

(19) Kneipp, K.; Kneipp, H.; Itzkan, I.; Dasari, R. R.; Feld, M. S. *Chem. Rev.* **1999**, *99* (10), 2957−2976.

(20) Saar, B. G.; Freudiger, C. W.; Reichman, J.; Stanley, C. M.; Holtom, G. R.; Xie, X. S. *Science* **2010**, *330* (6009), 1368−1370.

(21) Camp, C. H., Jr; Cicerone, M. T. *Nat. Photonics* **2015**, *9* (5), 295−305.

(22) Zumbusch, A.; Holtom, G. R.; Xie, X. S. *Phys. Rev. Lett.* **1999**, *82* (20), 4142.

(23) Min, W.; Freudiger, C. W.; Lu, S.; Xie, X. S. *Annu. Rev. Phys. Chem.* **2011**, *62* (1), 507−530.

(24) Cheng, J.; Volkmer, A.; Book, L. D.; Xie, X. S. *J. Phys. Chem. B* **2001**, *105* (7), 1277−1280.

(25) Ozeki, Y.; Umemura, W.; Otsuka, Y.; Satoh, S.; Hashimoto, H.; Sumimura, K.; Nishizawa, N.; Fukui, K.; Itoh, K. *Nat. Photonics* **2012**, *6* (12), 845−851.

(26) Camp, C. H., Jr; Lee, Y. J.; Heddleston, J. M.; Hartshorn, C. M.; Walker, A. R. H.; Rich, J. N.; Lathia, J. D.; Cicerone, M. T. *Nat. Photonics* **2014**, *8* (8), 627−634.

(27) Kee, T. W.; Cicerone, M. T. *Opt. Lett.* **2004**, *29* (23), 2701.

(28) Mitchell, A. L.; Gajjar, K. B.; Theophilou, G.; Martin, F. L.; Martin-Hirsch, P. L. *J. Biophoton.* **2014**, *7* (3−4), 153−165.

(29) Aslam, M. A.; Xue, C.; Liu, M.; Wang, K.; Cui, D. *Eng. Lett.* **2021**, *29* (1), EL_29_1_02.

(30) Bahreini, M.; Hosseinzadegan, A.; Rashidi, A.; Miri, S. R.; Mirzaei, H. R.; Hajian, P. *Talanta* **2019**, *204*, 826−832.

(31) Avram, L.; Iancu, S. D.; Stefancu, A.; Moisoiu, V.; Colnita, A.; Marconi, D.; Donca, V.; Buzdugan, E.; Craciun, R.; Leopold, N.; Crisan, N.; Coman, I.; Crisan, D. *J. Clin. Med.* **2020**, *9* (1), 212.

(32) Lin, X.; Wang, L.; Lin, H.; Lin, D.; Lin, J.; Liu, X.; Qiu, S.; Xu, Y.; Chen, G.; Feng, S. *J. Biophotonics* **2019**, *12* (4), No. e201800327.

(33) Nargis, H. F.; Nawaz, H.; Bhatti, H. N.; Jilani, K.; Saleem, M. *Spectrochim. Acta, Part A* **2021**, *246*, 119034.

(34) Lin, D.; Wang, Y.; Wang, T.; Zhu, Y.; Lin, X.; Lin, Y.; Feng, S. *Anal. Bioanal. Chem.* **2020**, *412* (7), 1611−1618.

(35) Moisoiu, V.; Stefancu, A.; Gulei, D.; Boitor, R.; Magdo, L.; Raduly, L.; Pasca, S.; Kubelac, P.; Mehterov, N.; Chis, V.; Simon, M.; Muresan, M.; Irimie, A. I.; Baciut, M.; Stiufiuc, R.; Pavel, I. E.; Achimas-Cadariu, P.; Ionescu, C.; Lazar, V.; Sarafian, V.; Notingher, I.; Leopold, N.; Berindan-Neagoe, I. *Int. J. Nanomed.* **2019**, *14*, 6165−6178.

(36) Kim, S.; Kim, T. G.; Lee, S. H.; Kim, W.; Bang, A.; Moon, S. W.; Song, J.; Shin, J.-H.; Yu, J. S.; Choi, S. *ACS Appl. Mater. Interfaces* **2020**, *12* (7), 7897−7904.

(37) Moisoiu, V.; Socaciu, A.; Stefancu, A.; Iancu, S. D.; Boros, I.; Alecsa, C. D.; Rachieriu, C.; Chiorean, A. R.; Eniu, D.; Leopold, N.; Socaciu, C.; Eniu, D. T. *Appl. Sci.* **2019**, *9* (4), 806.

(38) Liu, K.; Jin, S.; Song, Z.; Jiang, L.; Ma, L.; Zhang, Z. *Vib. Spectrosc.* **2019**, *100*, 177−184.

(39) Shin, H.; Oh, S.; Hong, S.; Kang, M.; Kang, D.; Ji, Y.; Choi, B. H.; Kang, K.-W.; Jeong, H.; Park, Y.; Hong, S.; Kim, H. K.; Choi, Y. *ACS Nano* **2020**, *14* (5), 5435−5444.

(40) Liu, K.; Jin, S.; Song, Z.; Jiang, L. *Spectrochim. Acta, Part A* **2020**, *226*, 117632.

(41) Ke, Z.-Y.; Ning, Y.-J.; Jiang, Z.-F.; Zhu, Y.; Guo, J.; Fan, X.-Y.; Zhang, Y.-B. *Lasers Med. Sci.* **2021**. DOI: 10.1007/s10103-021-03275-4

(42) Hu, D.; Xu, X.; Zhao, Z.; Li, C.; Tian, Y.; Liu, Q.; Shao, B.; Chen, S.; Zhao, Y.; Li, L.; Bi, H.; Chen, A.; Fu, C.; Cui, X.; Zeng, Y. *Spectrochim. Acta, Part A* **2021**, *247*, 119108.

(43) Chen, S.; Zhu, S.; Cui, X.; Xu, W.; Kong, C.; Zhang, Z.; Qian, W. *Biomed. Opt. Express* **2019**, *10* (7), 3533−3544.

(44) Maitra, I.; Morais, C. L. M.; Lima, K. M. G.; Ashton, K. M.; Date, R. S.; Martin, F. L. *J. Biophotonics* **2020**, *13* (3), No. e201960132.

(45) Sahu, A.; Gera, P.; Malik, A.; Nair, S.; Chaturvedi, P.; Murali Krishna, C. *J. Biophotonics* **2019**, *12* (8), No. e201800334.

(46) Falamas, A.; Faur, C. I.; Ciupe, S.; Chirila, M.; Rotaru, H.; Hedesiu, M.; Cinta Pinzaru, S. *Spectrochim. Acta, Part A* **2021**, *252*, 119477.

(47) Ghosh, A.; Raha, S.; Dey, S.; Chatterjee, K.; Roy Chowdhury, A.; Barui, A. *Analyst* **2019**, *144* (4), 1309−1325.

(48) de Oliveira, M. A. S.; Campbell, M.; Afify, A. M.; Huang, E. C.; Chan, J. W. *Biomed. Opt. Express* **2019**, *10* (9), 4411−4421.

(49) Xia, L.; Lu, J.; Chen, Z.; Cui, X.; Chen, S.; Pei, D. *Nanomedicine* **2021**, *32*, 102328.

(50) Liang, X.; Miao, X.; Xiao, W.; Ye, Q.; Wang, S.; Lin, J.; Li, C.; Huang, Z. *Int. J. Nanomed.* **2020**, *15*, 2303−2314.

(51) Giamougiannis, P.; Morais, C. L. M.; Grabowska, R.; Ashton, K. M.; Wood, N. J.; Martin-Hirsch, P. L.; Martin, F. L. *Anal. Bioanal. Chem.* **2021**, *413* (3), 911−922.

(52) Perumal, J.; Mahyuddin, A. P.; Balasundaram, G.; Goh, D.; Fu, C. Y.; Kazakeviciute, A.; Dinish, U. S.; Choolani, M.; Olivo, M. *Cancer Manage. Res.* **2019**, *11*, 1115−1124.

(53) Ralbovsky, N. M.; Halámková, L.; Wall, K.; Anderson-Hanley, C.; Lednev, I. K. *J. Alzheimer's Dis.* **2019**, *71* (4), 1351−1359.

(54) Ryzhikova, E.; Ralbovsky, N. M.; Sikirzhytski, V.; Kazakov, O.; Halamkova, L.; Quinn, J.; Zimmerman, E. A.; Lednev, I. K. *Spectrochim. Acta, Part A* **2021**, *248*, 119188.

(55) Carlomagno, C.; Cabinio, M.; Picciolini, S.; Gualerzi, A.; Baglio, F.; Bedoni, M. *J. Biophotonics* **2020**, *13* (3), No. e201960033.

(56) Ryzhikova, E.; Ralbovsky, N. M.; Halámková, L.; Celmins, D.; Malone, P.; Molho, E.; Quinn, J.; Zimmerman, E. A.; Lednev, I. K. *Appl. Sci.* **2019**, *9* (16), 3256.

(57) Zhang, Q.-J.; Chen, Y.; Zou, X.-H.; Hu, W.; Lin, X.-L.; Feng, S.-Y.; Chen, F.; Xu, L.-Q.; Chen, W.-J.; Wang, N. *J. Biophotonics* **2019**, *12* (8), No. e201900012.

(58) Moström, P.; Ahlén, E.; Imberg, H.; Hansson, P.-O.; Lind, M. *BMJ. Open Diab Res. Care* **2017**, *5* (1), No. e000342.

(59) Freckmann, G. *Journal of Laboratory Medicine* **2020**, *44* (2), 71−79.

(60) Kang, J. W.; Park, Y. S.; Chang, H.; Lee, W.; Singh, S. P.; Choi, W.; Galindo, L. H.; Dasari, R. R.; Nam, S. H.; Park, J.; So, P. T. C. *Science Advances* **2020**, *6* (4), No. eaay5206.

(61) Ju, J.; Hsieh, C.-M.; Tian, Y.; Kang, J.; Chia, R.; Chang, H.; Bai, Y.; Xu, C.; Wang, X.; Liu, Q. *ACS Sens* **2020**, *5* (6), 1777−1785.

(62) Lundsgaard-Nielsen, S. M.; Pors, A.; Banke, S. O.; Henriksen, J. E.; Hepp, D. K.; Weber, A. *PLoS One* **2018**, *13* (5), No. e0197134.

(63) Pleus, S.; Schauer, S.; Jendrike, N.; Zschornack, E.; Link, M.; Hepp, K. D.; Haug, C.; Freckmann, G. *J. Diabetes Sci. Technol.* **2021**, *15* (1), 11−18.

(64) Paolillo, F. R.; Mattos, V. S.; de Oliveira, A. O.; Guimaraes, F. E. G.; Bagnato, V. S.; de Castro Neto, J. C. *Journal of Biophotonics* **2019**, *12* (1), No. e201800162.

(65) WHO. *World Malaria Report*, 2015; http://www.who.int/malaria/publications/world-malaria-report-2015/report/en/ (accessed 2021-05-10).

(66) Chen, K.; Perlaki, C.; Xiong, A.; Preiser, P.; Liu, Q. *IEEE J. Sel. Top. Quantum Electron.* **2016**, *22* (4), 179−187.

(67) Patel, S. K.; Rajora, N.; Kumar, S.; Sahu, A.; Kochar, S. K.; Krishna, C. M.; Srivastava, S. *Anal. Chem.* **2019**, *91* (11), 7054−7062.

(68) Ngo, H. T.; Strobbia, P.; Vohra, P.; Freedman, E.; Indrasekara, A. S. D. S.; Lee, W. T.; Taylor, S. M.; Vo-Dinh, T. A Nanophotonic-Based Assay for Point-of-Care Medical Diagnostics of Malaria in Low and Middle Income Countries. In *Optics and Biophotonics in Low-Resource Settings V*; International Society for Optics and Photonics, 2019; Vol. *10869*, p 108690V.

(69) Wang, W.; Dong, R.; Gu, D.; He, J.; Yi, P.; Kong, S.-K.; Ho, H.-P.; Loo, J. F.-C.; Wang, W.; Wang, Q. *Adv. Med. Sci.* **2020**, *65* (1), 86−92.

(70) Mhlanga, N.; Domfe, T.; Skepu, A.; Ntho, T. A. *J. Raman Spectrosc.* **2020**, *51* (12), 2416−2424.

(71) Laupland, K. B.; Valiquette, L. T. *Canadian Journal of Infectious Diseases and Medical Microbiology* **2013**, *24* (3), 125−128.

(72) Lagier, J.-C.; Edouard, S.; Pagnier, I.; Mediannikov, O.; Drancourt, M.; Raoult, D. *Clin. Microbiol. Rev.* **2015**, *28* (1), 208−236.

(73) Carrigan, S. D.; Scott, G.; Tabrizian, M. *Clin. Chem.* **2004**, *50* (8), 1301−1314.

(74) Aguero-Rosenfeld, M. E.; Kalantarpour, F.; Baluch, M.; Horowitz, H. W.; McKenna, D. F.; Raffalli, J. T.; Hsieh, T.; Wu, J.; Dumler, J. S.; Wormser, G. P. *J. Clin. Microbiol.* **2000**, *38* (2), 635−638.

(75) Confield, L. R.; Black, G. P.; Wilson, B. C.; Lowe, D. J.; Theakstone, A. G.; Baker, M. J. *Anal. Methods* **2021**, *13* (2), 157−168.

(76) Wang, X.; Ma, L.; Sun, S.; Liu, T.; Zhou, H.; Liu, X.; Guan, M. *Anal. Methods* **2021**, *13* (15), 1823−1831.

(77) Klag, T.; Cantara, G.; Sechtem, U.; Athanasiadis, A. *IInfect Dis Rep* **2016**, *8* (1), 6213.

(78) Lee, T.; Lim, J.; Park, K.; Lim, E.-K.; Lee, J.-J. *ACS Sens* **2020**, *5* (10), 3099−3108.

(79) De Plano, L. M.; Fazio, E.; Rizzo, M. G.; Franco, D.; Carnazza, S.; Trusso, S.; Neri, F.; Guglielmino, S. P. P. *J. Immunol. Methods* **2019**, *465*, 45−52.

(80) Chang, K.-W.; Cheng, H.-W.; Shiue, J.; Wang, J.-K.; Wang, Y.-L.; Huang, N.-T. *Anal. Chem.* **2019**, *91* (17), 10988−10995.

(81) Han, Y.-Y.; Lin, Y.-C.; Cheng, W.-C.; Lin, Y.-T.; Teng, L.-J.; Wang, J.-K.; Wang, Y.-L. *Sci. Rep.* **2020**, *10*, 12538.

(82) Yi, X.; Song, Y.; Xu, X.; Peng, D.; Wang, J.; Qie, X.; Lin, K.; Yu, M.; Ge, M.; Wang, Y.; Zhang, D.; Yang, Q.; Wang, M.; Huang, W. E. *Anal. Chem.* **2021**, *93* (12), 5098−5106.

(83) Verma, T.; Majumdar, S.; Yadav, S.; Ahmed, S. M.; Umapathy, S.; Nandi, D. *Analyst* **2021**, *146* (12), 4022−4032.

(84) Yarbakht, M.; Pradhan, P.; Köse-Vogel, N.; Bae, H.; Stengel, S.; Meyer, T.; Schmitt, M.; Stallmach, A.; Popp, J.; Bocklitz, T. W.; Bruns, T. *Anal. Chem.* **2019**, *91* (17), 11116−11121.

(85) Chen, X.; Tang, M.; Liu, Y.; Huang, J.; Liu, Z.; Tian, H.; Zheng, Y.; de la Chapelle, M. L.; Zhang, Y.; Fu, W. *Microchim. Acta* **2019**, *186* (2), 102.

(86) Hernández-Cedillo, A.; García-Valdivieso, M. G.; Hernández-Arteaga, A. C.; Patiño-Marín, N.; Vértiz-Hernández, Á. A.; José-Yacamán, M.; Navarro-Contreras, H. R. *Oral Dis* **2019**, *25* (6), 1627−1633.

(87) Tong, D.; Chen, C.; Zhang, J.; Lv, G.; Zheng, X.; Zhang, Z.; Lv, X. *Photodiagn. Photodyn. Ther.* **2019**, *28*, 248−252.

(88) Ditta, A.; Nawaz, H.; Mahmood, T.; Majeed, M. I.; Tahir, M.; Rashid, N.; Muddassar, M.; Al-Saadi, A. A.; Byrne, H. J. *Spectrochim. Acta, Part A* **2019**, *221*, 117173.

(89) Naseer, K.; Amin, A.; Saleem, M.; Qazi, J. *Spectrochim. Acta, Part A* **2019**, *206*, 197−201.

(90) Butowt, R.; Bilinska, K. *ACS Chem. Neurosci.* **2020**, *11* (9), 1200−1203.

(91) Carlomagno, C.; Bertazioli, D.; Gualerzi, A.; Picciolini, S.; Banfi, P. I.; Lax, A.; Messina, E.; Navarro, J.; Bianchi, L.; Caronni, A.; Marenco, F.; Monteleone, S.; Arienti, C.; Bedoni, M. *Sci. Rep.* **2021**, *11* (1), 4943.

(92) Yin, G.; Li, L.; Lu, S.; Yin, Y.; Su, Y.; Zeng, Y.; Luo, M.; Ma, M.; Zhou, H.; Orlandini, L.; Yao, D.; Liu, G.; Lang, J. *J. Raman Spectrosc.* **2021**, *52* (5), 949−958.

(93) Tian, M.; Lei, L.; Xie, W.; Yang, Q.; Li, C. M.; Liu, Y. *Sens. Actuators, B* **2019**, *282*, 96−103.

(94) Bishop, J. D.; Hsieh, H. V.; Gasperino, D. J.; Weigl, B. H. *Lab Chip* **2019**, *19* (15), 2486−2499.

(95) Yadav, S.; Sadique, M. A.; Ranjan, P.; Kumar, N.; Singhal, A.; Srivastava, A. K.; Khan, R. *ACS Appl. Bio Mater.* **2021**, *4* (4), 2974−2995.

(96) Liu, H.; Dai, E.; Xiao, R.; Zhou, Z.; Zhang, M.; Bai, Z.; Shao, Y.; Qi, K.; Tu, J.; Wang, C.; Wang, S. *Sens. Actuators, B* **2021**, *329*, 129196.

(97) Sturgis, C. D.; Nassar, D. L.; D'Antonio, J. A.; Raab, S. S. *Am. J. Clin. Pathol.* **2000**, *114* (2), 197−202.

(98) Avwioro, G. *JPCS* **2011**, *1*, 24−34.

(99) Pantanowitz, L.; Evans, A.; Pfeifer, J.; Collins, L.; Valenstein, P.; Kaplan, K.; Wilbur, D.; Colgan, T. *J. Pathol Inform* **2011**, *2* (1), 36.

(100) Kirkegaard, T.; Edwards, J.; Tovey, S.; McGlynn, L. M.; Krishna, S. N.; Mukherjee, R.; Tam, L.; Munro, A. F.; Dunne, B.; Bartlett, J. M. S. *Histopathology* **2006**, *48* (7), 787−794.

(101) Cordero, E.; Rüger, J.; Marti, D.; Mondol, A. S.; Hasselager, T.; Mogensen, K.; Hermann, G. G.; Popp, J.; Schie, I. W. *J. Biophotonics* **2020**, *13* (2), No. e201960025.

(102) Placzek, F.; Cordero Bautista, E.; Kretschmer, S.; Wurster, L. M.; Knorr, F.; González-Cerdas, G.; Erkkilä, M. T.; Stein, P.; Ataman, Ç.; Hermann, G. G.; Mogensen, K.; Hasselager, T.; Andersen, P. E.; Zappe, H.; Popp, J.; Drexler, W.; Leitgeb, R. A.; Schie, I. W. *Analyst* **2020**, *145* (4), 1445−1456.

(103) Lyng, F. M.; Traynor, D.; Nguyen, T. N. Q.; Meade, A. D.; Rakib, F.; Al-Saady, R.; Goormaghtigh, E.; Al-Saad, K.; Ali, M. H. *PLoS One* **2019**, *14* (2), No. e0212376.

(104) Koya, S. K.; Brusatori, M.; Yurgelevic, S.; Huang, C.; Werner, C. W.; Kast, R. E.; Shanley, J.; Sherman, M.; Honn, K. V.; Maddipati, K. R.; Auner, G. W. *Prostaglandins Other Lipid Mediators* **2020**, *151*, 106475.

(105) Shang, L.-W.; Ma, D.-Y.; Fu, J.-J.; Lu, Y.-F.; Zhao, Y.; Xu, X.-Y.; Yin, J.-H. *Biomed. Opt. Express* **2020**, *11* (7), 3673−3683.

(106) Ali, N.; Quansah, E.; Köhler, K.; Meyer, T.; Schmitt, M.; Popp, J.; Niendorf, A.; Bocklitz, T. *Translational Biophotonics* **2019**, *1* (1−2), No. e201900003.

(107) Sarri, B.; Canonge, R.; Audier, X.; Simon, E.; Wojak, J.; Caillol, F.; Cador, C.; Marguet, D.; Poizat, F.; Giovannini, M.; Rigneault, H. *Sci. Rep.* **2019**, *9* (1), 10052.

(108) Hollon, T. C.; Pandian, B.; Adapa, A. R.; Urias, E.; Save, A. V.; Khalsa, S. S. S.; Eichberg, D. G.; D'Amico, R. S.; Farooq, Z. U.; Lewis, S.; Petridis, P. D.; Marie, T.; Shah, A. H.; Garton, H. J. L.; Maher, C. O.; Heth, J. A.; McKean, E. L.; Sullivan, S. E.; Hervey-Jumper, S. L.; Patil, P. G.; Thompson, B. G.; Sagher, O.; McKhann, G. M.; Komotar, R. J.; Ivan, M. E.; Snuderl, M.; Otten, M. L.; Johnson, T. D.; Sisti, M. B.; Bruce, J. N.; Muraszko, K. M.; Trautman, J.; Freudiger, C. W.; Canoll, P.; Lee, H.; Camelo-Piragua, S.; Orringer, D. A. *Nat. Med.* **2020**, *26* (1), 52−58.

(109) Eichberg, D. G.; Shah, A. H.; Di, L.; Semonche, A. M.; Jimsheleishvili, G.; Luther, E. M.; Sarkiss, C. A.; Levi, A. D.; Gultekin, S. H.; Komotar, R. J.; Ivan, M. E. *J. Neurosurg.* **2021**, *134* (1), 137−143.

(110) Doherty, T.; McKeever, S.; Al-Attar, N.; Murphy, T.; Aura, C.; Rahman, A.; O'Neill, A.; Finn, S. P.; Kay, E.; Gallagher, W. M.; Watson, R. W. G.; Gowen, A.; Jackman, P. *Analyst* **2021**, *146* (13), 4195−4211.

(111) Zhang, L.; Wu, Y.; Zheng, B.; Su, L.; Chen, Y.; Ma, S.; Hu, Q.; Zou, X.; Yao, L.; Yang, Y.; Chen, L.; Mao, Y.; Chen, Y.; Ji, M. *Theranostics* **2019**, *9* (9), 2541−2554.

(112) Rodner, E.; Bocklitz, T.; von Eggeling, F.; Ernst, G.; Chernavskaia, O.; Popp, J.; Denzler, J.; Guntinas-Lichius, O. *Head & Neck* **2018**, *41* (1), 116−121.

(113) Feng, X.; Fox, M. C.; Reichenberg, J. S.; Lopes, F. C. P. S.; Sebastian, K. R.; Markey, M. K.; Tunnell, J. W. *Biomed. Opt. Express* **2019**, *10* (1), 104−118.

(114) Feng, X.; Fox, M. C.; Reichenberg, J. S.; Lopes, F. C. P. S.; Sebastian, K. R.; Dunn, A. K.; Markey, M. K.; Tunnell, J. W. *J. Biophotonics* **2020**, *13* (2), No. e201960109.

(115) Liu, C.; Wu, B.; Sordillo, L. A.; Boydston-White, S.; Sriramoju, V.; Zhang, C.; Beckman, H.; Zhang, L.; Pei, Z.; Shi, L.; Alfano, R. R. *J. Cancer Metastasis Treat.* **2019**, *5*, 4.

(116) Shahmoradian, S. H.; Lewis, A. J.; Genoud, C.; Hench, J.; Moors, T. E.; Navarro, P. P.; Castaño-Díez, D.; Schweighauser, G.; Graff-Meyer, A.; Goldie, K. N.; Sütterlin, R.; Huisman, E.; Ingrassia, A.; Gier, Y. de; Rozemuller, A. J. M.; Wang, J.; Paepe, A. D.; Erny, J.; Staempfli, A.; Hoernschemeyer, J.; Großerüschkamp, F.; Niedieker, D.; El-Mashtoly, S. F.; Quadri, M.; Van IJcken, W. F. J.; Bonifati, V.; Gerwert, K.; Bohrmann, B.; Frank, S.; Britschgi, M.; Stahlberg, H.; Van de Berg, W. D. J.; Lauer, M. E. *Nat. Neurosci.* **2019**, *22* (7), 1099−1109.

(117) Moors, T. E.; Maat, C. A.; Niedieker, D.; Mona, D.; Petersen, D.; Timmermans-Huisman, E.; Kole, J.; El-Mashtoly, S. F.; Spycher, L.; Zago, W.; Barbour, R.; Mundigl, O.; Kaluza, K.; Huber, S.; Hug, M. N.; Kremer, T.; Ritter, M.; Dziadek, S.; Geurts, J. J. G.; Gerwert, K.; Britschgi, M.; van de Berg, W. D. *Acta Neuropathol.* **2021**, *142* (3), 423−448.

(118) Röhr, D.; Boon, B. D. C.; Schuler, M.; Kremer, K.; Hoozemans, J. J. M.; Bouwman, F. H.; El-Mashtoly, S. F.; Nabers, A.; Großerueschkamp, F.; Rozemuller, A. J. M.; Gerwert, K. *Acta Neuropathol. Commun.* **2020**, *8* (1), 222.

(119) Lochocki, B.; Boon, B. D. C.; Verheul, S. R.; Zada, L.; Hoozemans, J. J. M.; Ariese, F.; de Boer, J. F. *Commun. Biol.* **2021**, *4*, 474.

(120) Lochocki, B.; Morrema, T. H. J.; Ariese, F.; Hoozemans, J. J. M.; de Boer, J. F. *Analyst* **2020**, *145* (5), 1724−1736.

(121) Cunha, R.; Lafeta, L.; Fonseca, E. A.; Barbosa, A.; Romano-Silva, M. A.; Vieira, R.; Jorio, A.; Malard, L. M. *Analyst* **2021**, *146* (9), 2945−2954.

(122) Ikenberg, H.; Bergeron, C.; Schmidt, D.; Griesser, H.; Alameda, F.; Angeloni, C.; Bogers, J.; Dachez, R.; Denton, K.; Hariri, J.; Keller, T.; von Knebel Doeberitz, M.; Neumann, H. H.; Puig-Tintore, L. M.; Sideri, M.; Rehm, S.; Ridder, R. *JNCI: Journal of the National Cancer Institute* **2013**, *105* (20), 1550−1557.

(123) Kitchener, H. C.; Blanks, R.; Dunn, G.; Gunn, L.; Desai, M.; Albrow, R.; Mather, J.; Rana, D. N.; Cubie, H.; Moore, C.; Legood, R.; Gray, A.; Moss, S. *Lancet Oncol.* **2011**, *12* (1), 56−64.

(124) McCrory, D. C.; Matchar, D. B.; Bastian, L.; Datta, S.; Hasselblad, V.; Hickey, J.; Myers, E.; Nanda, K. *Evid. Rep. Technol. Assess (Summ)* **1999**, *5*, 1−6.

(125) Walboomers, J. M.; Jacobs, M. V.; Manos, M. M.; Bosch, F. X.; Kummer, J. A.; Shah, K. V.; Snijders, P. J.; Peto, J.; Meijer, C. J.; Muñoz, N. HJ *J. Pathol.* **1999**, *189* (1), 12−19.

(126) Ronco, G.; Giorgi-Rossi, P.; Carozzi, F.; Confortini, M.; Palma, P. D.; Del Mistro, A.; Ghiringhello, B.; Girlando, S.; Gillio-Tos, A.; De Marco, L.; Naldoni, C.; Pierotti, P.; Rizzolo, R.; Schincaglia, P.; Zorzi, M.; Zappa, M.; Segnan, N.; Cuzick, J. *Lancet Oncol.* **2010**, *11* (3), 249−257.

(127) Ferlay, J.; Shin, H.-R.; Bray, F.; Forman, D.; Mathers, C.; Parkin, D. M. *Int. J. Cancer* **2010**, *127* (12), 2893−2917.

(128) Traynor, D.; Behl, I.; O'Dea, D.; Bonnier, F.; Nicholson, S.; O'Connell, F.; Maguire, A.; Flint, S.; Galvin, S.; Healy, C. M.; Martin, C. M.; O'Leary, J. J.; Malkin, A.; Byrne, H. J.; Lyng, F. M. *Nat. Protoc.* **2021**, *16* (7), 3716−3735.

(129) Duraipandian, S.; Traynor, D.; Kearney, P.; Martin, C.; O'Leary, J. J.; Lyng, F. M. *Sci. Rep.* **2018**, *8*, 15048.

(130) Traynor, D.; Martin, C. M.; White, C.; Reynolds, S.; D'Arcy, T.; O'Leary, J. J.; Lyng, F. M. *Cancers* **2021**, *13* (9), 2008.

(131) Karunakaran, V.; Saritha, V. N.; Joseph, M. M.; Nair, J. B.; Saranya, G.; Raghu, K. G.; Sujathan, K.; Kumar, K. S.; Maiti, K. K. *Nanomedicine* **2020**, *29*, 102276.

(132) Aljakouch, K.; Hilal, Z.; Daho, I.; Schuler, M.; Krauß, S. D.; Yosef, H. K.; Dierks, J.; Mosig, A.; Gerwert, K.; El-Mashtoly, S. F. *Anal. Chem.* **2019**, *91* (21), 13900−13906.

(133) Slater, D. N.; Rice, S.; Stewart, R.; Melling, S. E.; Hewer, E. M.; Smith, J. H. F. *Cytopathology* **2005**, *16* (4), 179−192.

(134) Herbert, A. *Cytopathology* **2005**, *16* (4), 165−166.

(135) Yosef, H. K.; Krauß, S. D.; Lechtonen, T.; Jütte, H.; Tannapfel, A.; Käfferlein, H. U.; Brüning, T.; Roghmann, F.; Noldus, J.; Mosig, A.; El-Mashtoly, S. F.; Gerwert, K. *Anal. Chem.* **2017**, *89* (12), 6893−6899.

(136) Babjuk, M.; Burger, M.; Zigeuner, R.; Shariat, S. F.; van Rhijn, B. W. G.; Compérat, E.; Sylvester, R. J.; Kaasinen, E.; Böhle, A.; Palou Redorta, J.; Rouprêt, M. *Eur. Urol.* **2013**, *64* (4), 639−653.

(137) Todenhöfer, T.; Hennenlotter, J.; Kühs, U.; Tews, V.; Gakis, G.; Aufderklamm, S.; Stenzl, A.; Schwentner, C. *Urology* **2012**, *79* (3), 620−625.

(138) Sullivan, P. S.; Chan, J. B.; Levin, M. R.; Rao, J. *Am. J. Transl Res.* **2010**, *2* (4), 412−440.

(139) Lotan, Y.; Roehrborn, C. G. *Urology* **2003**, *61* (1), 109−118.

(140) Yafi, F. A.; Brimo, F.; Steinberg, J.; Aprikian, A. G.; Tanguay, S.; Kassouf, W. *Urologic Oncology: Seminars and Original Investigations* **2015**, *33* (2), 66.e25−66.e31.

(141) Krauß, S. D.; Roy, R.; Yosef, H. K.; Lechtonen, T.; El-Mashtoly, S. F.; Gerwert, K.; Mosig, A. *Journal of Biophotonics* **2018**, *11* (10), No. e201800022.

(142) Krauß, S. D.; Yosef, H. K.; Lechtonen, T.; Jütte, H.; Tannapfel, A.; Käfferlein, H. U.; Brüning, T.; Roghmann, F.; Noldus, J.; El-Mashtoly, S. F.; Gerwert, K.; Mosig, A. *J. Chemom.* **2018**, *32* (1), No. e2973.

(143) Benderska-Söder, N.; Hovanec, J.; Pesch, B.; Goebell, P. J.; Roghmann, F.; Noldus, J.; Rabinovich, J.; Wichert, K.; Gleichenhagen, J.; Käfferlein, H. U.; Köhler, C. U.; Johnen, G.; Kernig, K.; Hakenberg, O.; Jahn, D.; Todenhöfer, T.; Stenzl, A.; Gleissner, J.; Gerwert, K.; El-Mashtoly, S.; Behrens, T.; Brüning, T.; Schmitz-Dräger, B. *J. Urologic Oncology: Seminars and Original Investigations* **2020**, *38* (12), 886−895.

(144) Falzone, L.; Salomone, S.; Libra, M. *Front. Pharmacol.* **2018**, *9*, 1300.

(145) Liu, Z.; Delavan, B.; Roberts, R.; Tong, W. *Trends Pharmacol. Sci.* **2017**, *38* (10), 852−872.

(146) Conway, J. R. W.; Carragher, N. O.; Timpson, P. *Nat. Rev. Cancer* **2014**, *14* (5), 314−328.

(147) El-Mashtoly, S. F.; Petersen, D.; Yosef, H. K.; Mosig, A.; Reinacher-Schick, A.; Kötting, C.; Gerwert, K. *Analyst* **2014**, *139* (5), 1155−1161.

(148) Aljakouch, K.; Lechtonen, T.; Yosef, H. K.; Hammoud, M. K.; Alsaidi, W.; Kötting, C.; Mügge, C.; Kourist, R.; El-Mashtoly, S. F.; Gerwert, K. *Angew. Chem., Int. Ed.* **2018**, *57* (24), 7250−7254.

(149) Sepp, K.; Lee, M.; Bluntzer, M. T. J.; Helgason, G. V.; Hulme, A. N.; Brunton, V. G. *J. Med. Chem.* **2020**, *63* (5), 2028−2034.

(150) El-Mashtoly, S. F. *J. Med. Chem.* **2020**, *63* (7), 3472−3474.

(151) Hu, F.; Shi, L.; Min, W. *Nat. Methods* **2019**, *16* (9), 830−842.

(152) Seidel, J.; Miao, Y.; Porterfield, W.; Cai, W.; Zhu, X.; Kim, S.-J.; Hu, F.; Bhattarai-Kline, S.; Min, W.; Zhang, W. *Chem. Commun.* **2019**, *55* (63), 9379−9382.

(153) Bae, K.; Zheng, W.; Ma, Y.; Huang, Z. *Anal. Chem.* **2020**, *92* (1), 740−748.

(154) Yosef, H. K.; Frick, T.; Hammoud, M. K.; Maghnouj, A.; Hahn, S.; Gerwert, K.; El-Mashtoly, S. F. *Analyst* **2018**, *143* (24), 6069−6078.

(155) Rammal, H.; Al Assaad, A.; Dosio, F.; Stella, B.; Maksimenko, A.; Mura, S.; Van Gulick, L.; Callewaert, M.; Desmaële, D.; Couvreur, P.; Morjani, H.; Beljebbar, A. *Nanomedicine* **2021**, *35*, 102404.

(156) Fu, D.; Zhou, J.; Zhu, W. S.; Manley, P. W.; Wang, Y. K.; Hood, T.; Wylie, A.; Xie, X. S. *Nat. Chem.* **2014**, *6* (7), 614−622.

(157) Dong, P.-T.; Zong, C.; Dagher, Z.; Hui, J.; Li, J.; Zhan, Y.; Zhang, M.; Mansour, M. K.; Cheng, J.-X. *Sci. Adv.* **2021**, *7* (2), No. eabd5230.

(158) Zhuge, M.; Huang, K.; Lee, H. J.; Jiang, Y.; Tan, Y.; Lin, H.; Dong, P.; Zhao, G.; Matei, D.; Yang, Q.; Cheng, J. *Adv. Sci.* **2021**, *8* (9), 2003136.

(159) Vanden-Hehir, S.; Tipping, W.; Lee, M.; Brunton, V.; Williams, A.; Hulme, A. *Nanomaterials* **2019**, *9* (3), 341.

(160) Vanden-Hehir, S.; Cairns, S. A.; Lee, M.; Zoupi, L.; Shaver, M. P.; Brunton, V. G.; Williams, A.; Hulme, A. N. *Biomacromolecules* **2019**, *20* (10), 4008−4014.

(161) Bugárová, N.; Annušová, A.; Bodík, M.; Šiffalovič, P.; Labudová, M.; Kajanová, I.; Zatovičová, M.; Pastoreková, S.; Majková, E.; Omastová, M. *Nanomedicine* **2020**, *30*, 102280.

(162) Jin, Q.; Fan, X.; Chen, C.; Huang, L.; Wang, J.; Tang, X. *Anal. Chem.* **2019**, *91* (6), 3784−3789.

(163) Herkenne, C.; Alberti, I.; Naik, A.; Kalia, Y. N.; Mathy, F.-X.; Préat, V.; Guy, R. H. *Pharm. Res.* **2008**, *25*, 87−103.

(164) Franzen, L.; Windbergs, M. *Adv. Drug Delivery Rev.* **2015**, *89*, 91−104.

(165) dos Santos, L.; Tippavajhala, V. K.; Mendes, T. O.; da Silva, M. G. P.; FáVero, P. P.; Téllez Soto, C. A.; Martin, A. A. *Vib. Spectrosc.* **2019**, *100*, 123−130.

(166) Caspers, P. J.; Nico, C.; Bakker Schut, T. C.; Sterke, J.; Pudney, P. D. A.; Curto, P. R.; Illand, A.; Puppels, G. J. *Transl. Biophoton.* **2019**, *1* (1−2), e201900004.

(167) Saar, B. G.; Contreras-Rojas, L. R.; Xie, X. S.; Guy, R. H. *Mol. Pharmaceutics* **2011**, *8* (3), 969−975.

(168) Wanjiku, B.; Yamamoto, K.; Klossek, A.; Schumacher, F.; Pischon, H.; Mundhenk, L.; Rancan, F.; Judd, M. M.; Ahmed, M.; Zoschke, C.; Kleuser, B.; Rühl, E.; Schäfer-Korting, M. *Anal. Chem.* **2019**, *91* (11), 7208−7214.

(169) Feizpour, A.; Marstrand, T.; Bastholm, L.; Eirefelt, S.; Evans, C. L. *J. Invest. Dermatol.* **2021**, *141* (2), 395−403.

(170) Pena, A.-M.; Chen, X.; Pence, I. J.; Bornschlögl, T.; Jeong, S.; Grégoire, S.; Luengo, G. S.; Hallegot, P.; Obeidy, P.; Feizpour, A.; Chan, K. F.; Evans, C. L. *Adv. Drug Delivery Rev.* **2020**, *153*, 147−168.

(171) Sarri, B.; Chen, X.; Canonge, R.; Grégoire, S.; Formanek, F.; Galey, J.-B.; Potter, A.; Bornschlögl, T.; Rigneault, H. *J. Controlled Release* **2019**, *308*, 190−196.

(172) Lin, P.; Ni, H.; Li, H.; Vickers, N. A.; Tan, Y.; Gong, R.; Bifano, T.; Cheng, J.-X. *Opt. Express* **2020**, *28* (20), 30210.

(173) Rangan, S.; Schulze, H. G.; Vardaki, M. Z.; Blades, M. W.; Piret, J. M.; Turner, R. F. B. *Analyst* **2020**, *145* (6), 2070−2105.

(174) Baradez, M.-O.; Biziato, D.; Hassan, E.; Marshall, D. *Front. Med.* **2018**, *5*, 47.

(175) Suhito, I. R.; Han, Y.; Ryu, Y.-S.; Son, H.; Kim, T.-H. *Biosens. Bioelectron.* **2021**, *178*, 113018.

(176) Hsu, C.-C.; Xu, J.; Brinkhof, B.; Wang, H.; Cui, Z.; Huang, W. E.; Ye, H. *Proc. Natl. Acad. Sci. U. S. A.* **2020**, *117* (31), 18412−18423.

(177) Hua, S.; Zhong, S.; Arami, H.; He, J.; Zhong, D.; Zhang, D.; Chen, X.; Qian, J.; Hu, X.; Zhou, M. *Adv. Funct. Mater.* **2021**, *31* (24), 2100468.

(178) Gala de Pablo, J.; Lindley, M.; Hiramatsu, K.; Goda, K. *Acc. Chem. Res.* **2021**, *54* (9), 2132−2143.

(179) Hiramatsu, K.; Ideguchi, T.; Yonamine, Y.; Lee, S.; Luo, Y.; Hashimoto, K.; Ito, T.; Hase, M.; Park, J.-W.; Kasai, Y.; Sakuma, S.; Hayakawa, T.; Arai, F.; Hoshino, Y.; Goda, K. *Sci. Adv.* **2019**, *5* (1), No. eaau0241.

(180) Hiramatsu, K.; Yamada, K.; Lindley, M.; Suzuki, K.; Goda, K. *Biomed. Opt. Express* **2020**, *11* (4), 1752.

(181) Suzuki, Y.; Kobayashi, K.; Wakisaka, Y.; Deng, D.; Tanaka, S.; Huang, C.-J.; Lei, C.; Sun, C.-W.; Liu, H.; Fujiwaki, Y.; Lee, S.; Isozaki, A.; Kasai, Y.; Hayakawa, T.; Sakuma, S.; Arai, F.; Koizumi, K.; Tezuka, H.; Inaba, M.; Hiraki, K.; Ito, T.; Hase, M.; Matsusaka, S.; Shiba, K.; Suga, K.; Nishikawa, M.; Jona, M.; Yatomi, Y.; Yalikun, Y.; Tanaka, Y.; Sugimura, T.; Nitta, N.; Goda, K.; Ozeki, Y. *Proc. Natl. Acad. Sci. U. S. A.* **2019**, *116* (32), 15842−15848.

(182) Nitta, N.; Iino, T.; Isozaki, A.; Yamagishi, M.; Kitahama, Y.; Sakuma, S.; Suzuki, Y.; Tezuka, H.; Oikawa, M.; Arai, F.; Asai, T.; Deng, D.; Fukuzawa, H.; Hase, M.; Hasunuma, T.; Hayakawa, T.; Hiraki, K.; Hiramatsu, K.; Hoshino, Y.; Inaba, M.; Inoue, Y.; Ito, T.; Kajikawa, M.; Karakawa, H.; Kasai, Y.; Kato, Y.; Kobayashi, H.; Lei, C.; Matsusaka, S.; Mikami, H.; Nakagawa, A.; Numata, K.; Ota, T.; Sekiya, T.; Shiba, K.; Shirasaki, Y.; Suzuki, N.; Tanaka, S.; Ueno, S.; Watarai, H.; Yamano, T.; Yazawa, M.; Yonamine, Y.; Di Carlo, D.; Hosokawa, Y.; Uemura, S.; Sugimura, T.; Ozeki, Y.; Goda, K. *Nat. Commun.* **2020**, *11*, 3452.

(183) Guo, S.; Beleites, C.; Neugebauer, U.; Abalde-Cela, S.; Afseth, N. K.; Alsamad, F.; Anand, S.; Araujo-Andrade, C.; Aškrabić, S.; Avci, E.; Baia, M.; Baranska, M.; Baria, E.; Batista de Carvalho, L. A. E.; de Bettignies, P.; Bonifacio, A.; Bonnier, F.; Brauchle, E. M.; Byrne, H. J.; Chourpa, I.; Cicchi, R.; Cuisinier, F.; Culha, M.; Dahms, M.; David, C.; Duponchel, L.; Duraipandian, S.; El-Mashtoly, S. F.; Ellis, D. I.; Eppe, G.; Falgayrac, G.; Gamulin, O.; Gardner, B.; Gardner, P.; Gerwert, K.; Giamarellos-Bourboulis, E. J.; Gizurarson, S.; Gnyba, M.; Goodacre, R.; Grysan, P.; Guntinas-Lichius, O.; Helgadottir, H.; Grošev, V. M.; Kendall, C.; Kiselev, R.; Kölbach, M.; Krafft, C.; Krishnamoorthy, S.; Kubryck, P.; Lendl, B.; Loza-Alvarez, P.; Lyng, F. M.; Machill, S.; Malherbe, C.; Marro, M.; Marques, M. P. M.; Matuszyk, E.; Morasso, C. F.; Moreau, M.; Muhamadali, H.; Mussi, V.; Notingher, I.; Pacia, M. Z.; Pavone, F. S.; Penel, G.; Petersen, D.; Piot, O.; Rau, J. V.; Richter, M.; Rybarczyk, M. K.; Salehi, H.; Schenke-Layland, K.; Schlücker, S.; Schosserer, M.; Schütze, K.; Sergo, V.; Sinjab, F.; Smulko, J.; Sockalingum, G. D.; Stiebing, C.; Stone, N.; Untereiner, V.; Vanna, R.; Wieland, K.; Popp, J.; Bocklitz, T. *Anal. Chem.* **2020**, *92* (24), 15745−15756.